Largest aftershock nucleation driven by afterslip during the 2014 Iquique sequence

Yuji Itoh[1,2,*], Anne Socquet[1], and Mathilde Radiguet[1]

[1]Univ. Grenoble Alpes, Univ. Savoie Mont Blanc, CNRS, IRD, Univ. Gustave Eiffel, ISTerre, 38000 Grenoble, France.

[2]Earthquake Research Institute, The University of Tokyo, Tokyo, Japan.

*Corresponding author: Yuji Itoh (yitoh@eri.u-tokyo.ac.jp)

Key Points:

- Global Positioning System captured crustal deformation during 27 hours between the 2014 Iquique mainshock and its largest aftershock
- The aseismic area south of the mainshock impeded the mainshock rupture, preventing simultaneous occurrence of the largest aftershock
- Cascading nucleation of the largest aftershock, highlighted by the increase in seismic moment release, is driven by early afterslip

Abstract (<= 150 words)

Various earthquake models predict that aseismic slip modulates the seismic rupture process but actual observations of such seismic-aseismic interaction are scarce. We analyze seismic and aseismic processes during the 2014 Iquique earthquake sequence. High-rate Global Positioning System (GPS) coordinates demonstrate that most of the afterslip is located downdip of the M 8.1 mainshock and is accompanied by aftershocks, both of which rapidly decay with time. An intriguing secondary afterslip peak is located ~120 km further south where the megathrust is known to creep at various time scales. This aseismic area likely acted as a barrier to the propagating mainshock rupture and delayed the occurrence of the M 7.6 largest aftershock, which eventually nucleated in this aseismic area. There, the seismic to aseismic moment ratio increased during the 27-hour interevent stage. This suggests that the cascading largest aftershock nucleation is driven by the in-situ afterslip.

Plain Language Summary

Subduction zone faults host both fast (regular earthquakes, seismic) and slow (aseismic) slip. Simulation models predict that slow slip can affect fast slip processes. We explored such an interaction taking place during the 2014 Iquique earthquake offshore northern Chile using observation data of crustal deformation by GPS and earthquakes. We discovered that the fast mainshock slip was terminated by a slowly slipping fault zone, which prevented the simultaneous occurrence of the largest aftershock. Furthermore, afterslip, one type of slow slip following the mainshock, helped the occurrence of the largest aftershock 27 hours after the mainshock. Therefore, the sequential occurrence of large earthquakes can be controlled by slowly slipping faults.

1 Introduction

Subduction zone megathrust faults host diverse slip behaviors. Seismic and aseismic slip are two complementary types (e.g., Scholz, 1998). Laboratory experiments and mechanical simulations of earthquake cycles demonstrate that aseismic and seismic processes commonly interact with each other in various manners. For example, the nucleation of numerical and laboratory earthquakes is associated with precursory seismic and aseismic processes (e.g., Cattania & Segall, 2021; Dieterich, 1992; McLaskey, 2019; Noda et al., 2013). Such seismic and aseismic interaction processes are often observed associated with large earthquakes as well. Short-term (a few days; e.g., Kato et al., 2012; Ohta et al., 2012) and long-term (a few months to a decade; Marill et al., 2021; Mavrommatis et al., 2014; Yokota & Koketsu, 2015) changes in geodetic coordinate series and seismic activity before the 2011 M_w 9.0 Tohoku earthquake have been interpreted in this regard. In addition, seismic ruptures are often terminated by an aseismic segment (e.g., model; Kaneko et al., 2010, observations; Nishikawa et al., 2019; Perfettini et al., 2010; Rolandone et al., 2018). Finally, laboratory earthquakes can interact via migrating aseismic creep fronts, and thus be responsible for delayed triggering (e.g., Cebry et al., 2022). In nature, aftershock occurrence is often controlled by afterslip (Klein et al., 2021; Perfettini et al., 2018). These theoretical and observational studies suggest that mechanically heterogeneous faults yield various scenarios of seismic-aseismic interactions.

The 2014 M 8.1 Iquique earthquake in northern Chile along the Nazca megathrust (Figure 1a) is also an excellent target for studying such seismic-aseismic interaction in nature. Long-term locking models illustrate a heterogeneous mosaic of locked and creeping areas (Jolivet et al., 2020; Li et al., 2015; Métois et al., 2016; Schurr et al., 2014). The 2014 event was preceded by short- (2-3 weeks) and long-term (8 months to years) precursory seismic and aseismic activities in and around the subsequent mainshock rupture area (Bedford et al., 2015; Boudin et al., 2022; Herman et al., 2016; Kato et al., 2016; Ruiz et al., 2014; Schurr et al., 2014; Socquet et al., 2017; Twardzik et al., 2022). Despite these previous studies, processes between the 2014 mainshock and the largest aftershock (M 7.6, Figure 1a), which we call "interevent" in this study, have so far remained unstudied. This largest aftershock occurred ~120 km south of the mainshock (Duputel et al., 2015; Hayes et al. 2014; Jara et al., 2018; Meng et al., 2015; Ruiz et al., 2014) and occurred 27 hours later. Resolving aseismic processes at such a short time scale is usually challenging because it requires high-rate GPS coordinates that are noisier than the standard daily coordinates. However, recent successful high-rate-GPS-based identification of early postseismic processes (e.g., Jiang et al., 2021; Liu et al., 2022; Miyazaki & Larson, 2008; Periollat et al. 2022; Tsang et al., 2019, Twardzik et al., 2021) suggest its applicability to the 2014 Iquique case. This study investigates source processes during the 2014 Iquique sequence by unveiling the early postseismic slip for a few days using high-rate GPS and comparing them with seismicity. Then, we discuss their implications for earthquake mechanics, particularly the role of aseismic megathrust in rupture segmentation and nucleation of large earthquakes.

2 Methods

2.1 High-rate GPS data analysis

2.1.1 GPS data cleaning

We employed 5-minute high-rate GPS coordinates processed by the Nevada Geodetic Laboratory (NGL; Blewitt et al., 2018; black in Figure S1). We removed coordinate fluctuations due to multipath (e.g., Bock et al., 2000; Itoh & Aoki, 2022; Ragheb et al., 2007) and diurnal variations using Seasonal-Trend decomposition using LOESS (STL) (Cleveland et al., 1990) with repeating periods of 23 hours and 55 minutes and 1 day, respectively (red and pink in Figure S1) from the 5-minute coordinate time series. Then, we removed common mode errors originating from fluctuations of the reference frame and satellite orbit errors (Wdowinski et al., 1997). We extracted common mode errors by stacking cleaned and despiked time series at 6 sites in the nodal direction of the mainshock and the largest aftershock, where little coseismic deformation is expected (Figure 1 and orange in Figure S1). We provide details of the cleaning procedure in Text S1.

2.1.2 Computation of displacements at four stages

After correcting the time series for the common modes, we extracted displacements associated with the mainshock, the interevent stage, the largest aftershock, and the 2-day post-largest-aftershock stages from these "cleaned" time series (blue in Figure S1). We fit a trajectory model (Figures 1c-e, S2a-c) between 5 days before and 30 days after the day of the mainshock.

Our trajectory model consists of step and logarithmic terms (Equation (S2) in Text S2), which represent coseismic static deformation and postseismic response assuming velocity-strengthening afterslip (Marone et al., 1991; Perfettini & Avouac, 2004; Perfettini et al., 2018), respectively. In the subsequent slip inversions, we used the cumulative displacements estimated using the trajectory model with time constants of the logarithmic term fitting fairly the “cleaned” data (Figures 1c-e, S2a-c; See Text S2 and Figures S3-S5 for details). Then, we carried out a moving median filter on the time series without the co-seismic steps to extract temporal evolution during the interevent stage (Figure 2a; see Text S3 for details). The moving median is non-parametric and therefore can keep more information from the original observations than the trajectory model predictions, which allows only for a monotonic change in the displacement (Figure S6). The window length of the median computation is 0.5 days. We obtained displacements during two interevent substages with an equal length (~13.5 hours) from the moving median time series.

2.2 Slip inversions

We employed the non-linear slip inversion code SDM (Wang et al., 2009, 2013a) to infer slip distribution during the two earthquakes, the interevent and the post-largest-aftershock stages. This allows us to depict the interplay of seismic and aseismic slip in a methodologically consistent manner, despite many published coseismic models (Boudin et al., 2022; Duputel et al., 2015; Hayes et al. 2014; Jara et al., 2018; Meng et al., 2015; Ruiz et al., 2014). We inverted the three components of GPS displacements weighted according to their formal errors (See Text S4 for details of interevent datasets). We used the homogeneous isotropic elastic half-space (Okada, 1992) and Slab2 fault geometry (Figure 1a; Hayes, 2018). We imposed a slip roughness constraint to regularize the inversion problem and we determined its strength using a trade-off curve of data misfit versus slip roughness (Figure S7-S8). We constrain the rake angle to be between 45 and 135 degrees. We used 30 GPa for rigidity to compute seismic moment and Coulomb Stress Change (CSC; King et al. 1994; Figure S9; See Text S5). For the incremental slip during the two interevent substages (Figure 2e-f), we found it necessary to additionally constrain the upper bound of slip because the incremental displacements derived from the moving median analysis are noisier than the cumulative displacements derived from the trajectory model fit (details in Text S4). As presented below, the inferred slips have multiple peaks and an overlap of seismic and aseismic slips. Hence, we carried out several tests to assess the robustness of the inversion results (Figures S10-S13). Also, we used models with different roughness to grasp robust slip features (Figures S7-S8). In particular, rougher solutions likely highlight the “minimum” extent of the slipping area.

2.3 Seismicity analysis

We employed McBrearty et al. (2019)’s seismicity catalog which lists many moderate aftershocks (Figures 1b, 2e-g, and 3a) among available catalogs (Sippl et al., 2018; Soto et al., 2019a). We carried out analyses of seismicity count (Figure 2c) and seismic moment (Figure 2d) for two regions. We divided the target region at 20.2°S within a range from 71.5°W to 70.0°W to highlight the contrast in seismicity at the mainshock (labeled North) and the largest aftershock (labeled South) latitudes. We computed the cumulative event count and seismic moment with a 0.002-day window. The seismic moment of each event is computed as $10^{1.5M_L+9.1}$ where M_L is a local magnitude from the catalog. The catalog we used tends to underestimate magnitude of large events, so we fixed the magnitude of an event 45 minutes before the largest aftershock from 5.6 to 6.1 (Soto et al., 2019a) (Table S1; Figure S14).

3 Results

3.1 Cumulative geodetic slip distributions at each stage

The static cumulative displacements at each stage demonstrate a coherent trenchward pattern (Figures 1 and S15), consistent with thrust faulting on the subduction interface (e.g., Jara et al., 2018; Hoffmann et al., 2018; Shrivastava et al., 2019). The inferred two coseismic slip patterns look similar to previous models which also used static offsets derived from high-rate GPS data (Figure 3a; Jara et al., 2018). The imaged interevent cumulative geodetic slip has some local maxima (blue contours in Figures 3a and S2e). The largest peak is located down-dip of the mainshock slip, a typical feature due to the depth-dependent change in megathrust rheology (e.g., Scholz, 1998). Another well-resolved peak is located south of the mainshock slip peak at seismogenic depth and is accompanied by moderate seismicity. One potentially missing slip patch could be located up-dip of the mainshock peak slip where a cluster of moderate seismicity is observed, some of which might be repeaters (Meng et al., 2015; Figures 4 and S16). Indeed, a slip patch appears up-dip of the mainshock peak when the mainshock peak slip zone is masked in the inversion (Figures S10c-d). Hence, an up-dip postseismic slip occurred, although it is not very large, contrary to another postseismic observation following a similar magnitude earthquake (e.g., Itoh et al., 2019; Miyazaki et al., 2004). The post-largest-aftershock geodetic slip has two peaks at both the North and South subareas, representing a continuation of the mainshock-induced postseismic slip superimposed with a postseismic slip enhanced by the largest aftershock (greens contours in Figures 3 and S15i).

The geodetically determined moment contains the aseismic slip on the interface slip as well as the seismic slip associated with aftershocks (e.g., Caballero et al., 2021; Twardzik et al., 2021, 2022). Our seismicity analysis shows that seismic moments during the interevent and the post-largest-aftershock stages are equivalent to M_w 6.2 and 5.8, about 3% and 1% of the corresponding geodetic moments M_w 7.2 and 7.1, respectively (Table S1; Figure S14). Hence, the early postseismic slip is substantially aseismic. This is much smaller than the early postseismic deformation of the 2015 Illapel earthquake during 12 hours (Twardzik et al., 2021). Seismic contributions at the North and South subareas are different and change with time (Table S1 and Figure S14).

Then, the confirmed aseismic slip contribution in the interevent and the post-largest-aftershock stages questions the overlap of the coseismic and aseismic slips (Figure 3a). This is because their overlap contradicts the consensus based on the rate-and-state friction law (e.g., Scholz, 1998) and some observations (Nishikawa et al., 2019; Perfettini et al., 2010; Rolandone et al., 2018). Our tests on the slip distribution robustness demonstrate that (1) Both the interevent (Figures S7b, S10a, S10c, and S13) and the largest aftershock coseismic data (Figures S12b and S12d) require moment release near the largest aftershock epicenter, hence, overlapping with each other to a certain extent, (2) The overlap of the mainshock and the interevent geodetic slip is likely due to the smoothing (Figures S10, S11c, and S12a), and (3) The largest aftershock slip needs to occur at and around its epicenter (Figures S11), but the post-largest-aftershock slip there is not strongly required by the data (Figures S12b and S12d); hence the overlap of the co- and post-largest-aftershock slip is favored but not strongly supported.

3.2 Temporal evolution during the interevent stage

The inferred geodetic slip during the two interevent substages demonstrates that slip rate decayed with time everywhere in the modeled area (Figures 2e-f, 3a, and S17), which is typical of afterslip response (e.g., Marone et al., 1991). The interevent slip is therefore essentially afterslip. The moving median time series illustrated as motograms (a spatial representation of the temporal evolution of horizontal motion; Figures 2a and S6) also support this decay; the emergence of interevent deformation right after the mainshock occurrence and their subsequent steady decay. This means that migration of the afterslip peak is not a dominant process at the interevent stage. Yet, coastal sites near the South area show a southward deflection of the motion during the late interevent stage, starting ~15 hours after the mainshock (Figure 2a), illustrated also in the displacement fields during the first and second substages (Figures 2e-f). The motion of sites in the North decays more rapidly than sites in the South (Figure 2a). These features suggest a temporal change in the slip pattern and/or perhaps a feeble southward migration of aseismic slip.

Unlike the geodetic slip, the evolution of moderate seismicity notably indicates a significant contrast between the North and South areas (Figures 2c-d and S18). In the mainshock area (North), the moment evolution inferred from seismicity shows very rapid decay. In contrast, in the largest aftershock area (South), the geodetic slip decays over time whereas a larger seismic moment release occurred during the second substage, dominated by the M 6.1 event (Figure 2d). The acceleration of seismicity count in this area (Figure 2c) is unclear because many small events are potentially missing in the catalog (Figures S19-S20). In this area, the seismic-to-geodetic moment ratio is less than 1% during the first substage, which increased to 37.5% subsequently (Figures 2d and S14 and Table S1). Hence, the interevent slip in the South subarea became more seismic with time. These features are very different from the 2015 Illapel case in which both early postseismic slip and aftershocks decay with time and one postseismic slip patch is 100% seismic due to some large aftershocks (Liu et al., 2022; Twardzik et al., 2021).

4 Discussion and Conclusions

4.1 Along-strike megathrust heterogeneity and rupture segmentation

The megathrust off-Iquique, where the southernmost interevent slip peak is found, has been creeping at different stages of the earthquake cycle (Fig. 4a). The afterslip lasted there at least for 9 months (Shrivastava et al., 2019). Various long-term interseismic locking models agree with the tendency of lower degrees of locking than the neighboring sections to the south and north (Figure 4b; e.g., Jolivet et al., 2020; Li et al., 2015; Métois et al., 2016; Schurr et al., 2014). The 8-month pre-mainshock aseismic transient (black contours in Figs. 3a-b; Socquet et al., 2017) overlaps with these aseismic slip regions. Hence, this aseismic slip area likely acted as a barrier to the southward propagation of the mainshock rupture (Duputel et al., 2015; Hayes et al. 2014; Jara et al., 2018; Meng et al., 2015) (Figures 3 and 4b) and prevented the immediate/simultaneous occurrence of the largest aftershock despite a positive mainshock CSC at the largest aftershock epicenter (Fig. S9a). Our interevent aseismic slip unambiguously confirms the spatiotemporal separation of the two big quakes by this aseismic barrier, which was indirectly proposed from an analysis of the post-largest-aftershock afterslip (Shrivastava et al., 2019). Similar sequential occurrences of large earthquakes intervened by afterslip have been reported elsewhere (e.g., Elliott et al., 2022; Klein et al., 2021; Miyazaki & Larson, 2008; Zhao et al., 2022).

Such creeping megathrust sections could be typically interpreted as zones of velocity-strengthening friction (Perfettini & Avouac, 2004), but this interpretation does not match with the overlap of the interevent aseismic slip, the 9-month afterslip patch (Shrivastava et al., 2019), and the largest aftershock coseismic slip. One possible interpretation would be that small seismic, velocity-weakening patches are embedded in the velocity-strengthening zone and they sometimes break altogether to form a large earthquake when they are critically loaded by surrounding creep. Locking of such small patches is not resolvable by land GNSS, so the area is imaged as an aseismic zone when the surrounding creep rate is low enough and behaves as an aseismic barrier (Figure 4; e.g., Avouac, 2015; Socquet et al., 2017). This may favor the termination of the 1877 $M_w \geq 8.5$ earthquake at off-Iquique (e.g., Vigny & Klein, 2022), but still does not exclude the possibility of rupture in this zone (Comte & Pardo, 1991; Kausel, 1986) (Figures 1a).

Another major controlling factor of faulting behavior is geometrical heterogeneity. Geometrical heterogeneity of faults with uniform velocity-weakening friction can realize collocation of seismic and aseismic slip (e.g., Cattania & Segall, 2021; Romanet et al. 2018). Wang and Bilek (2011) proposed that rugged faults due to seamount subduction favor slow creep more than large earthquakes. Off-Iquique, along-strike changes in gravity anomaly (Jara et al., 2018; Maksymowicz et al., 2018; Molina et al., 2021), spatial distribution of subparallel spray faults along the megathrust (Cubas et al., 2022), small seamounts on the megathrust interface (Geersen et al., 2015), local high slab topography (Storch et al., 2023) and Iquique ridge on the incoming Nazca plate have been reported (Figures 1a and S21). These observations imply that the off-Iquique megathrust has a more heterogeneous geometry and overburden stress than the neighbor segments along-strike. Such geometrical features might also be responsible for the complex mosaic of the aseismic and seismic processes there, in addition to the frictional heterogeneity.

The other two aseismic slip patches allow us to depict the mechanical characteristics of the megathrust north of the mainshock and down-dip of the largest aftershock (Figure 4). To the north of the mainshock latitude, aseismic slip before and after the mainshock overlap. Excess fluid pressure along the megathrust there may prevent the accumulation of elastic strain (Ma et al., 2022). The possible termination of the 1877 rupture is located there (Figure 1a) where long-term locking rates were inferred to be low (Jolivet et al., 2020; Li et al., 2015; Métois et al. 2016; Schurr et al., 2014). We speculate that the megathrust north of the mainshock peak is a persistent aseismic barrier (Figures 3b and 4b). The interevent aseismic slip patch down-dip of the largest aftershock overlaps with the 8-month pre-mainshock slip at greater depth (Figure 4a). The locking rate is also small there (Figure 4b). This patch at great depth could be controlled by the persistent creep controlled by ductile fault rheology (e.g., Scholz, 1998). This patch is away from the mainshock peak, so the increase of aseismic slip rate following the mainshock was perhaps triggered dynamically, similar to remotely triggered afterslip/slow slips by large earthquakes (e.g., Rolandone et al., 2018; Wallace et al., 2018).

4.2 Evolution of seismic-aseismic interaction toward the largest aftershock

The revealed temporal evolution of the interevent processes hints at the preparation processes of the largest aftershock. The interevent slip at the forthcoming largest aftershock area becomes more seismic with time (Figures 2c-d and 2g). Notably, the M 6.1 event 45 minutes before the largest aftershock occurred only 32km away from the largest aftershock epicenter (Soto et al., 2019a). We interpret these seismic characteristics as an indication of a cascade-up process of the largest aftershock nucleation at small seismic patches (e.g., Ellsworth & Bulut, 2018; Kato & Ben-Zion, 2021; McLaskey, 2019). In this regard, the negative CSC due to the interevent slip in the largest aftershock epicentral area probably reflects a cumulative stress drop associated with the nucleation (Figure S9b). Instantaneous stress loading during the interevent stage due to the cascading seismicity should have a much shorter spatial wavelength and hence the contribution of these moderate earthquakes is smeared out in the slip inversion. Actually, the stress perturbation by the interevent slip is much smaller than the mainshock (Figure S9), but those values depend largely on the inversion protocol, particularly, the strength of the roughness constraint, so we only interpret the sign of CSC here.

Contrary to the larger seismic moment release during the second substage, the interevent slip quickly decayed throughout the interevent stage (Figure 2e-f; Figure S14). Numerical models usually demonstrate an acceleration of precursor aseismic slip as a part of the nucleation processes (e.g., Cattania & Segall, 2021; Dieterich, 1992; Noda et al., 2013). Therefore, our decelerating interevent aseismic slip unlikely represents the largest aftershock's nucleation phase. However, it reveals that the aftershock occurrence may be prompted/favored by the preceding interevent aseismic slip that reduces the interface strength in the same area (Noda et al., 2013). Hence, our interevent aseismic slip likely acted as a stress-loading driver destabilizing the largest aftershock fault. This loading of the largest aftershock fault perhaps started with the 8-month pre-mainshock slow slip (Figure 4; Socquet et al., 2017) and the mainshock-induced slip rate increase was necessary to critically destabilize the largest aftershock area. We conclude that the nucleation of the largest aftershock is explained as the rate-dependent cascade-up model describing such a mixed-mode nucleation (Kato & Ben-Zion, 2021; McLaskey, 2019).

Another intriguing question relates to the delayed occurrence of the largest aftershock. Our analysis does not quantitatively explain the timing of this delay. Such delay is sometimes controlled by migrating slow slip (Ariyoshi et al., 2019; Cebry et al., 2022), but our seismic and aseismic observations do not support it as the dominant process (Figures 2a and 2e-g). Determination of the timing of large aftershocks is, hence, still an unresolved issue even after revealing the nucleation mechanism.

Acknowledgments

The authors declare no conflicts of interest. We appreciate Roland Burgmann and four anonymous reviewers of this or an earlier version manuscript for their thoughtful reviews.

Discussion with Jorge Jara, Zaccaria El Yousfi, Ian McBrearty, Taku Ueda, Michel Bouchon, Satoshi Ide, Jean-Philippe Avouac, and Sylvain Barbot was fruitful. Nadaya Cubas and Hui Huang provided us with the results of Cubas et al. (2022) and Meng et al. (2015), respectively. Aubin Tsapong helped check the quality of raw GPS observations. Geoffrey Blewitt answered our questions on their data processing strategy at NGL. We used Generic Mapping Tools (Wessel et al., 2013) to draw the figures. English check of an earlier version manuscript by James Hollingsworth helped improve the manuscript. Y.I. is a Japan Society for the Promotion of Science (JSPS) Overseas Research Fellow. This study is supported by Japan Society for the Promotion of Science (JSPS) Overseas Research Fellowships and KAKENHI 21K14007 and 21K03694 (YI) and ERC CoG 865963 DEEP-trigger (AS).

Open Research

We processed only published results/data and no new data were produced. The GPS coordinates (Blewitt et al., 2018) are available from Nevada Geodetic Laboratory (2022). The seismicity catalog of Soto et al. (2019a) is available from Soto et al. (2019b). The gravity anomaly (Sandwell et al., 2014) and topography (Smith & Sandwell, 1997) data are available from Scripps Institution of Oceanography (2022). The inversion code SDM (Wang et al., 2009, 2013a) is available from Wang et al. (2013b). We used a Fortran 90 translation of the DC3D subroutine (Okada, 1992) provided by Miyashita (2020). We made our slip distribution available in xxx (ready at publication).

References

Ariyoshi, K., Ampuero, J. P., Bürgmann, R., Matsuzawa, T., Hasegawa, A., Hino, R., & Hori, T. (2019). Quantitative relationship between aseismic slip propagation speed and frictional properties. *Tectonophysics*, 767, 128151. https://doi.org/10.1016/j.tecto.2019.06.021

Avouac, J. P. (2015). From geodetic imaging of seismic and aseismic fault slip to dynamic modeling of the seismic cycle. *Annual Review of Earth and Planetary Sciences*, 43, 233-271. https://doi.org/10.1146/annurev-earth-060614-105302

Bedford, J., Moreno, M., Schurr, B., Bartsch, M., & Oncken, O. (2015), Investigating the final seismic swarm before the Iquique-Pisagua 2014 Mw 8.1 by comparison of continuous GPS and seismic foreshock data. *Geophysical Research Letters*, 42, 3820–3828. https://doi.org/10.1002/2015GL063953

Blewitt, G., Hammond, W. C., & Kreemer, C. (2018). Harnessing the GPS data explosion for interdisciplinary science. *Eos, 99.* https://doi.org/10.1029/2018EO104623

Bock, Y., Nikolaidis, R. M., de Jonge, P. J., & Bevis, M. (2000). Instantaneous geodetic positioning at medium distances with the Global Positioning System. *Journal of Geophysical Research: Solid Earth* 105, 28223–28253. https://doi.org/10.1029/2000JB900268

Boudin, F., et al. (2022). Slow slip events precursory to the 2014 Iquique Earthquake, revisited with long-base tilt and GPS records, *Geophysical Journal International* 228, 2092–2121. https://doi.org/10.1093/gji/ggab425

Caballero, E., Chounet, A., Duputel, Z., Jara, J., Twardzik, C., & Jolivet, R. (2021). Seismic and aseismic fault slip during the initiation phase of the 2017 M_W = 6.9 Valparaíso earthquake. *Geophysical Research Letters*, 48, e2020GL091916. https://doi.org/10.1029/2020GL091916

Cattania, C., & Segall, P. (2021). Precursory slow slip and foreshocks on rough faults. *Journal of Geophysical Research: Solid Earth* 126, e2020JB020430. https://doi.org/10.1029/2020JB020430

Cebry, S. B. L., Ke, C. Y., Shreedharan, S. Marone, C., Kammer, D. S., McLaskey, G. C. (2022). Creep fronts and complexity in laboratory earthquake sequences illuminate delayed earthquake triggering. *Nature Communications*, 13, 6839. https://doi.org/10.1038/s41467-022-34397-0

Cleveland, R. B., Cleveland, W. S., McRae, J. E., & Terpenning, I. (1990). STL: A seasonal-trend decomposition procedure based on loess. *Journal of Official Statistics,* 6, 3–73

Comte, D., & Pardo, M. (1991). Reappraisal of great historical earthquakes in the northern Chile and southern Peru seismic gaps. *Natural Hazards*, 4, 23–44. https://doi.org/10.1007/BF00126557

Cubas, N., Agard, P., & Tissandier, R. (2022). Earthquake ruptures and topography of the Chilean margin controlled by plate interface deformation. *Solid Earth* 13, 779–792. https://doi.org/10.5194/se-13-779-2022

DeMets, C., Gordon, R. G., & Argus, D. F. (2010). Geologically current plate motions. *Geophysical Journal International,* 181, 1–80. https://doi.org/10.1111/j.1365-246X.2009.04491.x

Dieterich, J. H. (1992). Earthquake nucleation on faults with rate-and state-dependent strength. *Tectonophysics*, 211, 115-134. https://doi.org/10.1016/0040-1951(92)90055-B

Duputel, Z., et al. (2015). The Iquique earthquake sequence of April 2014: Bayesian modeling accounting for prediction uncertainty, *Geophysical Research Letter,s* 42, 7949–7957. https://doi.org/10.1002/2015GL065402

Elliott, J. L., Grapenthin, R., Parameswaran, R. M., Xiao, Z., Freymueller, J. T., & Fusso, L. (2022). Cascading rupture of a megathrust. *Science Advances*, 8, eabm4131. https://doi.org/10.1126/sciadv.abm4131

Ellsworth, W. L., & Bulut, F. (2018). Nucleation of the 1999 Izmit earthquake by a triggered cascade of foreshocks. *Nature Geoscience,* 11, 531–535. https://doi.org/10.1038/s41561-018-0145-1

Geersen, J., Ranero, C., Barckhausen, U., & Reichert, C. (2015), Subducting seamounts control interplate coupling and seismic rupture in the 2014 Iquique earthquake area. *Nature Communications,* 6, 8267. https://doi.org/10.1038/ncomms9267

Herman, M. W., Furlong, K. P., Hayes, G. P., & Benz, H. M. (2016). Foreshock triggering of the 1 April 2014 Mw 8.2 Iquique, Chile, earthquake. *Earth and Planetary Science Letters*, 447, 119-129. https://doi.org/10.1016/j.epsl.2016.04.020

Hayes, G. (2018). Slab2 - A comprehensive subduction zone geometry model. *U.S. Geological Survey data release*.

Hayes, G., et al. (2014). Continuing megathrust earthquake potential in Chile after the 2014 Iquique earthquake. *Nature,* 512, 295–298. https://doi.org/10.1038/nature13677

Hoffmann, F., Metzger, S., Moreno, M., Deng, Z., Sippl, C., Ortega-Culaciati, F., & Oncken, O. (2018). Characterizing afterslip and ground displacement rate increase following the 2014 Iquique-Pisagua M_w 8.1 earthquake, Northern Chile. *Journal of Geophysical Research: Solid Earth*, 123, 4171–4192. https://doi.org/10.1002/2017JB014970

Ito, Y., et al. (2013). Episodic slow slip events in the Japan subduction zone before the 2011 Tohoku-Oki earthquake. *Tectonophysics*, 600, 14-26. https://doi.org/10.1016/j.tecto.2012.08.022

Itoh, Y., & Aoki, Y. (2022). On the performance of position-domain sidereal filter for 30-s kinematic GPS to mitigate multipath errors. *Earth, Planets and Space,* 74, 23. https://doi.org/10.1186/s40623-022-01584-8

Itoh, Y., Nishimura, T., Ariyoshi, K., & Matsumoto, H. (2019). Interplate slip following the 2003 Tokachi-oki earthquake from ocean bottom pressure gauge and land GNSS data. *Journal of Geophysical Research: Solid Earth*, 124, 4205–4230. https://doi.org/10.1029/2018JB016328

Jara, J., et al. (2018). Kinematic study of Iquique 2014 Mw 8.1 earthquake: Understanding the segmentation of the seismogenic zone. *Earth and Planetary Science Letters,* 503, 131-143. https://doi.org/10.1016/j.epsl.2018.09.025

Jiang, J., Klein, E., & Bock, Y. (2021). Coevolving early afterslip and aftershock signatures of a San Andreas fault rupture. *Science Advances*, 7, eabc1606 https://doi.org/10.1126/sciadv.abc1606

Jolivet, R., Simons, M., Duputel, Z., Olive, J.-A., Bhat, H. S., & Bletery, Q. (2020). Interseismic loading of subduction megathrust drives long-term uplift in Northern Chile. *Geophysical Research Letters,* 47, e2019GL085377. https://doi.org/10.1029/2019GL085377

Kaneko, Y., Avouac, J.-P. & Lapusta, N. (2010). Towards inferring earthquake patterns from geodetic observations of interseismic coupling. *Nature Geosciences,* 3, 363–369. https://doi.org/10.1038/ngeo843

Kato, A., & Ben-Zion, Y. (2021). The generation of large earthquakes. *Nature Reviews Earth & Environment* 2, 26–39. https://doi.org/10.1038/s43017-020-00108-w

Kausel, E. (1986). Los terremotos de agosto de 1868 y mayo de 1877 que afectaron el sur del Perú y norte de Chile. Boletín de la Academia Chilena de Ciencias 3, 8–13

Kato, A., Fukuda, J., Kumazawa, T., & Nakagawa, S. (2016). Accelerated nucleation of the 2014 Iquique, Chile Mw 8.2 Earthquake. *Scientific Reports,* 6, 24792 https://doi.org/10.1038/srep24792

Kato, A., Obara, K., Igarashi, T., Tsuruoka, H., Nakagawa, S., & Hirata, N. (2012) Propagation of Slow Slip Leading Up to the 2011 M_w 9.0 Tohoku-Oki Earthquake. *Science* 335, 705-708. https://doi.org/10.1126/science.1215141

King, G. C. P., Stein, S. S., Lin, J. (1994). Static stress changes and the triggering of earthquakes. *Bulletin of Seismological Society of America.* 84, 935–953. https://doi.org/10.1785/BSSA0840030935

Klein, E. (2021). Interplay of seismic and a-seismic deformation during the 2020 sequence of Atacama, Chile. *Earth and Planetary Science Letters* 570, 117081. https://doi.org/10.1016/j.epsl.2021.117081

Li, S., Moreno, M., Bedford, J., Rosenau, M., Oncken, O. (2015). Revisiting viscoelastic effects on interseismic deformation and locking degree: A case study of the Peru-North Chile subduction zone. *Journal of Geophysical Research: Solid Earth* 120, 4522–4538. https://doi.org/10.1002/2015JB011903

Liu, K., Geng, J., Wen, Y., Ortega-Culaciati, F., & Comte, D. (2022). Very early postseismic deformation following the 2015 Mw 8.3 Illapel earthquake, Chile revealed from kinematic GPS. *Geophysical Research Letters*, 49, e2022GL098526. https://doi.org/10.1029/2022GL098526

Ma, B., et al., (2022). Megathrust reflectivity reveals the updip limit of the 2014 Iquique earthquake rupture. *Nature Communications* 13, 3969. https://doi.org/10.1038/s41467-022-31448-4

Maksymowicz, A., Ruiz, J., Vera, E., Contreras-Reyes, E., Ruiz, S., Arraigada, C., Bonvalot, S., & Bascuñan, S. (2018). Heterogeneous structure of the Northern Chile marine forearc and its implications for megathrust earthquakes. *Geophysical Journal International* 215, 1080–1097. https://doi.org/10.1093/gji/ggy325

Marill, L., Marsan, D., Socquet, A., Radiguet, M., Cotte, N., & Rousset, B., (2021). Fourteen-year acceleration along the Japan Trench. *Journal of Geophysical Research: Solid Earth* 126, e2020JB021226. https://doi.org/10.1029/2020JB021226

Marone, C. J., Scholz, C. H., & Bilham, R. (1991). On the mechanics of earthquake afterslip, *Journal of Geophysical Research: Solid Earth* 96, 8441–8452. https://doi.org/10.1029/91JB00275

Mavrommatis, A. P., Segall, P., & Johnson, K. M. (2014). A decadal-scale deformation transient prior to the 2011 M_w 9.0 Tohoku-oki earthquake, *Geophysical Research Letters*, 41, 4486–4494. https://doi.org/10.1002/2014GL060139

McBrearty, I. W., Gomberg, J., Delorey, A. A., & Johnson, P. A. (2019). Earthquake Arrival Association with Backprojection and Graph Theory. *Bulletin of Seismological Society of America* 109, 2510–2531. https://doi.org/10.1785/0120190081

McLaskey, G. C. (2019). Earthquake Initiation From Laboratory Observations and Implications for Foreshocks. *Journal of Geophysical Research: Solid Earth,* 124, 12882–12904. https://doi.org/10.1029/2019JB018363

Meng, L., Huang, H., Bürgmann, R., Ampuero, J.-P., & Strader, A. (2015). Dual megathrust slip behaviors of the 2014 Iquique earthquake sequence. *Earth and Planetary Science Letters* 411, 177-187. https://doi.org/10.1016/j.epsl.2014.11.041

Métois, M., Vigny, C., & Socquet, A. (2016). Interseismic Coupling, Megathrust Earthquakes and Seismic Swarms Along the Chilean Subduction Zone (38°–18°S). *Pure and Applied Geophysics* 173, 1431–1449. https://doi.org/10.1007/s00024-016-1280-5

Miyashita, T. (2020). DC3D.f90: January 14, 2020 Release [Software] Github https://github.com/hydrocoast/DC3D.f90

Miyazaki, S., & Larson, K. M. (2008). Coseismic and early postseismic slip for the 2003 Tokachi-oki earthquake sequence inferred from GPS data. *Geophysical Research Letters* 35, L04302. https://doi.org/10.1029/2007GL032309

Miyazaki, S., Segall, P., Fukuda, J., & Kato, T. (2004). Space time distribution of afterslip following the 2003 Tokachi-oki earthquake: Implications for variations in fault zone frictional properties. *Geophysical Research Letters*, 31, L06623, https://doi.org/10.1029/2003GL019410

Molina, D., Tassara, A., Abarca, R., Melnick, D., & Madella, A. (2021). Frictional segmentation of the Chilean megathrust from a multivariate analysis of geophysical, geological, and geodetic data. *Journal of Geophysical Research: Solid Earth*, 126, e2020JB020647 https://doi.org/10.1029/2020JB020647

Nevada Geodetic Laboratory (2022). [Dataset] http://geodesy.unr.edu/

Nishikawa, T., Matsuzawa, T., Ohta, K., Nishimura, T. & Ide, S. (2019). The slow earthquake spectrum in the Japan Trench illuminated by the S-net seafloor observatories. *Science* 365, 808-813. https://doi.org/10.1126/science.aax5618

Noda, H., Nakatani, M., & Hori, T. (2013), Large nucleation before large earthquakes is sometimes skipped due to cascade-up—Implications from a rate and state simulation of faults with hierarchical asperities, *Journal of Geophysical Research: Solid Earth*, 118, 2924– 2952. https://doi.org/10.1002/jgrb.50211

Ohta, Y., et al. (2012). Geodetic constraints on afterslip characteristics following the March 9, 2011, Sanriku-oki earthquake, Japan. *Geophysical Research Letters*, 39, L16304, https://doi.org/10.1029/2012GL052430

Okada, Y. (1992). Internal deformation due to shear and tensile faults in a half-space. *Bulletin of Seismological Society of America,* 82, 1018–1040. https://doi.org/10.1785/BSSA0820021018

Perfettini, H., & Avouac, J. P. (2004). Postseismic relaxation driven by brittle creep: A possible mechanism to reconcile geodetic measurements and the decay rate of aftershocks, application to the Chi-Chi earthquake, Taiwan. *Journal of Geophysical Research: Solid Earth*, 109, B02304. https://doi.org/10.1029/2003JB002488

Perfettini, H., et al. (2010). Seismic and aseismic slip on the Central Peru megathrust. *Nature* 465, 78–81. https://doi.org/10.1038/nature09062

Perfettini, H., Frank, W. B., Marsan, D, & Bouchon, M. (2018). A model of aftershock migration driven by afterslip. *Geophysical Research Letters,* 45, 2283– 2293. https://doi.org/10.1002/2017GL076287

Periollat, A., Radiguet, M., Weiss, J., Twardzik, C., Amitrano, D., Cotte, N., Marill, L., & Socquet, A. (2022). Transient brittle creep mechanism explains early postseismic phase of the 2011 Tohoku-Oki megathrust earthquake: Observations by high-rate GPS solutions. *Journal of Geophysical Research: Solid Earth,* 127, e2022JB024005. https://doi.org/10.1029/2022JB024005

Ragheb, A. E., Clarke, P. J., & Edwards, S. J. (2007). GPS sidereal filtering: Coordinate- and carrier-phase-level strategies. *Journal of Geodesy,* 81, 325–335. https://doi.org/10.1007/s00190-006-0113-1

Rolandone, F., et al., (2018). Areas prone to slow slip events impede earthquake rupture propagation and promote afterslip. *Science Advances,* 4, eaao6596. https://doi.org/10.1126/sciadv.aao6596

Romanet, P., Bhat, H. S., Jolivet, R., & Madariaga, R. (2018). Fast and slow slip events emerge due to fault geometrical complexity. *Geophysical Research Letters*, 45, 4809– 4819. https://doi.org/10.1029/2018GL077579

Ruiz, S., Metois, M., Fuenzalida, A., Ruiz, J., Leyton, F., Grandin, R., Vigny, C., Madariaga, R., & Campos, J. (2014). Intense foreshocks and a slow slip event preceded the 2014 Iquique Mw 8.1 earthquake. *Science,* 345, 1165-1169. https://doi.org/10.1126/science.1256074

Sandwell, D. T., Müller, R. D., Smith, W. H. F., Garcia, E., & Francis, R. (2014). New global marine gravity model from CryoSat-2 and Jason-1 reveals buried tectonic structure. *Science*, 346, 65-67. https://doi.org/10.1126/science.1258213

Scholz, C. (1998). Earthquakes and friction laws. *Nature,* 391, 37–42 https://doi.org/10.1038/34097

Scripps Institution of Oceanography (2022). EXTRACT XYZ GRID - TOPOGRAPHY OR GRAVITY. V19.1 and V29.1 for topography and gravity, respectively [Dataset] https://topex.ucsd.edu/cgi-bin/get_data.cgi

Schurr, B., et al. (2014). Gradual unlocking of plate boundary controlled initiation of the 2014 Iquique earthquake. *Nature,* 512, 299–302. https://doi.org/10.1038/nature13681

Shrivastava, M. N., González, G., Moreno, M., Soto, H., Schurr, B., Salazar, P., Báez, J. C. (2019). Earthquake segmentation in northern Chile correlates with curved plate geometry. *Scientific Reports,* 9, 4403. https://doi.org/10.1038/s41598-019-40282-6

Sippl, C., Schurr, B., Asch, G., & Kummerow, J. (2018). Seismicity structure of the northern Chile forearc from >100,000 double-difference relocated hypocenters. *Journal of Geophysical Research: Solid Earth*, 123, 4063– 4087. https://doi.org/10.1002/2017JB015384

Smith, W. H. F., & Sandwell, D. T. (1997). Global seafloor topography from satellite altimetry and ship depth soundings. *Science* 277, 1957-1962. https://doi.org/10.1126/science.277.5334.1956

Socquet, A., et al. (2017). An 8 month slow slip event triggers progressive nucleation of the 2014 Chile megathrust, *Geophysical Research Letters,* 44, 4046–4053. https://doi.org/10.1002/2017GL073023

Soto, H., Sippl, C., Schurr, B., Kummerow, J., Asch, G., Tilmann, F., Comte, D., Ruiz, S., & Oncken, O. (2019a). Probing the northern Chile megathrust with seismicity: the 2014 M8.1 iquique earthquake sequence. *Journal of Geophysical Research: Solid Earth,* 124, 12935–12954. https://doi.org/10.1029/2019JB017794

Soto, H., Sippl, C., Schurr, B., Kummerow, J., Asch, G., Tilmann, F., Comte, D., Ruiz, S., & Oncken, O. (2019b). Catalogue of Hypocenters for the 2014 M8.1 Iquique Earthquake Sequence, recorded by IPOC (plus additional) seismic stations. [Dataset] *GFZ Data Services*. https://doi.org/10.5880/GFZ.4.1.2019.009

Storch, I., Buske, S., Victor, P., & Oncken, O. (2023). A topographic depression on the subducting Nazca plate controls the April 1st 2014 M8. 1 Iquique earthquake rupture in Northern Chile. *Tectonophysics*, 847, 229684.

Tsang, L. L. H., et al. (2019). Imaging rapid early afterslip of the 2016 Pedernales earthquake, Ecuador. *Earth and Planetary Science Letters*, 524, 115724. https://doi.org/10.1016/j.epsl.2019.115724

Twardzik, C., Duputel, Z., Jolivet, R., Klein, E., & Rebischung, P. (2022). Bayesian inference on the initiation phase of the 2014 Iquique, Chile, earthquake. *Earth and Planetary Science Letters,* 600, 117835. https://doi.org/10.1016/j.epsl.2022.117835

Twardzik, C., Vergnolle, M., Sladen, A., & Tsang, L. L. H. (2021). Very early identification of a bimodal frictional behavior during the post-seismic phase of the 2015 Mw 8.3 Illapel, Chile, earthquake. *Solid Earth*, 12, 2523–2537. https://doi.org/10.5194/se-12-2523-2021

Vigny, C., & Klein, E. (2022). The 1877 megathrust earthquake of North Chile two times smaller than thought? A review of ancient articles. *Journal of South American Earth Sciences*, 117, 103878. https://doi.org/10.1016/j.jsames.2022.103878

Wallace, L. M., Hreinsdóttir, S., Ellis, S., Hamling, I., D'Anastasio, E., & Denys, P. (2018). Triggered slow slip and afterslip on the southern Hikurangi subduction zone following the Kaikōura earthquake. *Geophysical Research Letters*, 45, 4710–4718. https://doi.org/10.1002/2018GL077385

Wang, K., & Bilek, S. L. (2011). Do subducting seamounts generate or stop large earthquakes? *Geology,* 39, 819–822. https://doi.org/10.1130/G31856.1

Wang, L., Wang, R., Roth, F., Enescu, B., Hainzl, S., & Ergintav, S. (2009). Afterslip and viscoelastic relaxation following the 1999 M 7.4 Izmit earthquake from GPS measurements, *Geophysical Journal International*, 178, 1220-1237. https://doi.org/10.1111/j.1365-246X.2009.04228.x

Wang, R., Diao, F., Hoechner, A. (2013a). *SDM – A geodetic inversion code incorporating with layered crust structure and curved fault geometry* Paper presented at General Assembly European Geosciences Union, Vienna, Austria. https://gfzpublic.gfz-potsdam.de/pubman/faces/ViewItemOverviewPage.jsp?itemId=item_1975902

Wang, R., Diao, F., Hoechner, A. (2013b). SDM – A geodetic inversion code incorporating with layered crust structure and curved fault geometry: [Software] ftp://ftp.gfz-potsdam.de/pub/home/turk/wang/

Wdowinski, S., Bock, Y., Zhang, J., Fang, P., & Genrich, J. (1997). Southern California permanent GPS geodetic array: Spatial filtering of daily positions for estimating coseismic and postseismic displacements induced by the 1992 Landers earthquake. *Journal of Geophysical Research: Solid Earth,* 102, 18057–18070. https://doi.org/10.1029/97JB01378

Wessel, P., Smith W. H. F., Scharroo, R., Luis, J., & Wobbe F. (2013). Generic Mapping Tools: Improved Version Released. *EOS*, 94, 409–410. https://doi.org/10.1002/2013EO450001.

Yokota, Y., & Koketsu, K. (2015). A very long-term transient event preceding the 2011 Tohoku earthquake. *Nature Communications*, 6, 5934. https://doi.org/10.1038/ncomms6934

Zhao, B., Bürgmann, R., Wang, D., Zhang, J., Yu, J., & Li, Q. (2022). Aseismic slip and recent ruptures of persistent asperities along the Alaska-Aleutian subduction zone. *Nature Communications*, 13, 3098. https://doi.org/10.1038/s41467-022-30883-7

References only in supporting information

Altamimi, Z., Métivier, L., Rebischung, P., Rouby, H., & Collilieux, X. (2017). ITRF2014 plate motion model. *Geophysical Journal International* 209, 1906–1912. https://doi.org/10.1093/gji/ggx136

Itoh, Y., Aoki, Y., & Fukuda, J. (2022). Imaging evolution of Cascadia slow-slip event using high-rate GPS. *Scientific Reports,* 12, 7179. https://doi.org/10.1038/s41598-022-10957-8

Pedregosa, F., et al. (2011). Scikit-learn: Machine learning in Python. *Journal of Machine Learning Research* **12**, 2825–2830.

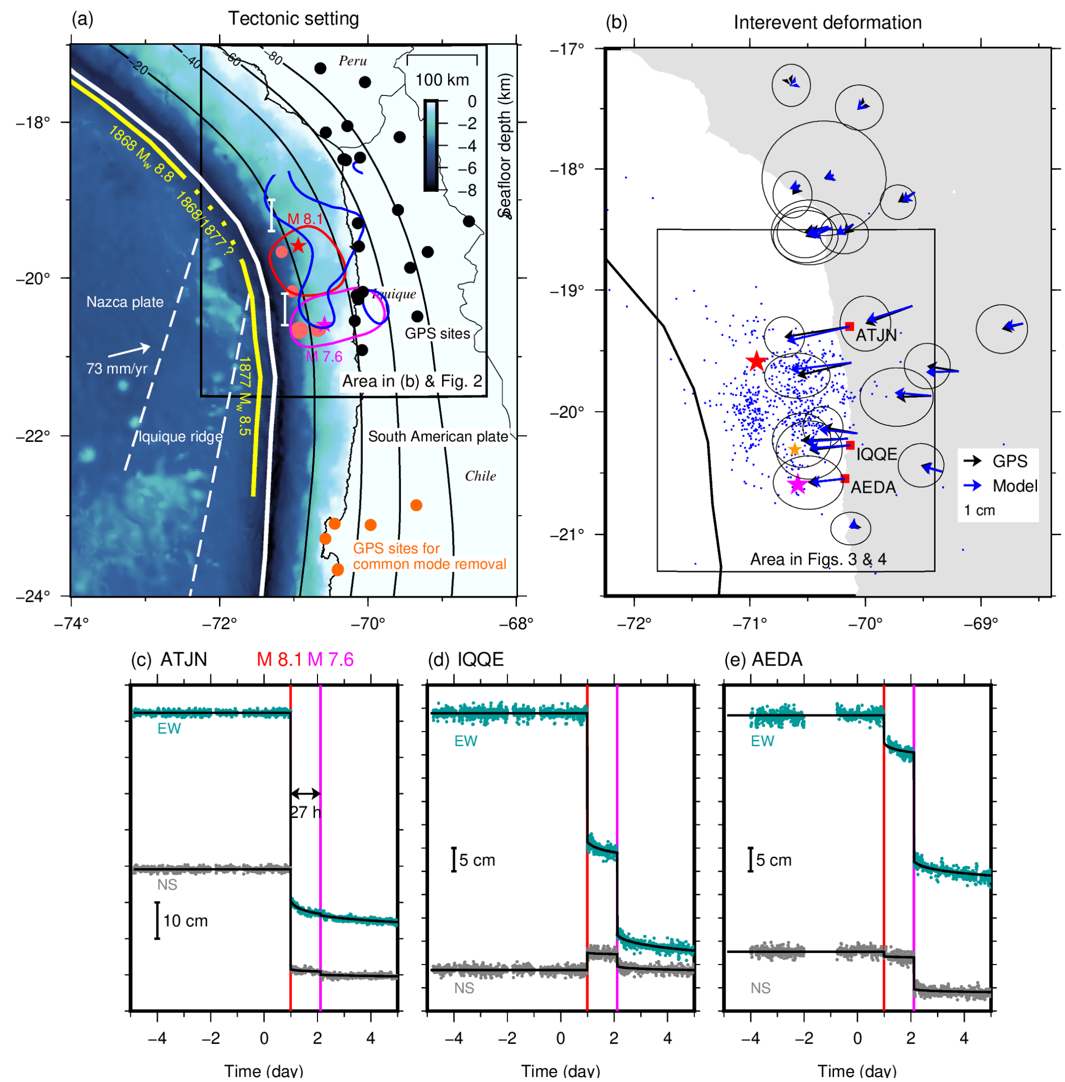

Figure 1. (a) Tectonic setting. Black and orange dots indicate GPS sites for deformation analysis and common mode noise extraction, respectively. Red and magenta stars indicate the epicenters of the 2014 Iquique mainshock and the largest aftershock, respectively (Soto et al., 2019a). Red, blue, and magenta curves outline slip areas of the mainshock, interevent afterslip, and the largest aftershock, respectively. A white arrow indicates the plate convergence motion (DeMets et al., 2010). Solid black contours indicate slab depth (Hayes, 2018). Yellow curves indicate rupture extension of large earthquakes with an uncertain section shown as a dotted curve (Comte & Pardo, 1991; Kausel, 1986). Red ovals indicate seismically imaged seamounts at the interface (Geersen et al., 2015). Two white bars offshore indicate the extent of inferred aseismic barriers. (b) Interevent horizontal GPS displacements with the model prediction from slip inversion (Figure 3a). Blue dots indicate interevent seismicity (McBrearty et al., 2019). The orange star indicates the M 6.1 epicenter (Soto et al., 2019a). (c-e) Cleaned 5-minute GPS coordinates at labeled sites (location in (b)) with trajectory model fits (black curves).

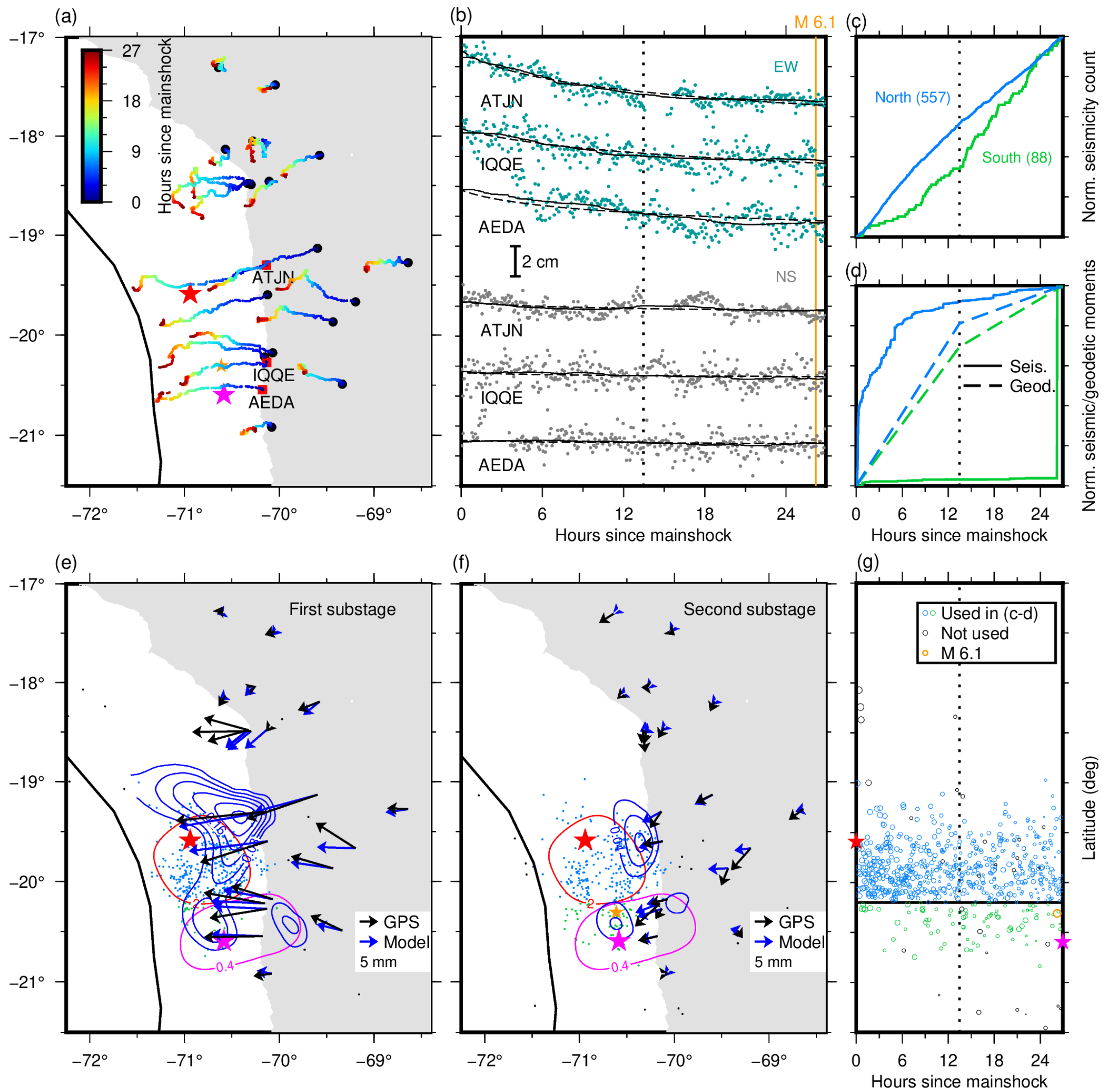

Figure 2. (a) Interevent GPS site motion drawn as motogram. (b) Interevent GPS coordinates (dots; location in (a)) and their moving median (0.5-day window; solid lines) and the trajectory model fit (Figures 1c-e; broken lines). A dotted vertical line shows the middle point of the interevent stage. (c) Normalized seismicity count (the total number in parentheses) in the two regions divided at 20.2°S as labeled. Events accounted for in the calculation (McBrearty et al., 2019) are shown in (e-f) with corresponding colors. (d) Same as (c) but with normalized seismic and geodetic moment as labeled (the actual values presented in Table S1). (e-f) Interevent afterslip snapshots (contour labels in m) by inverting incremental displacements (black vectors; see (b)). Displacement error ellipses are trimmed for clarity. Displacements at sites north of 19°S are not inverted. See Figures 1 and 3 for other elements. (g) Interevent seismicity (open circles scaled with magnitude).

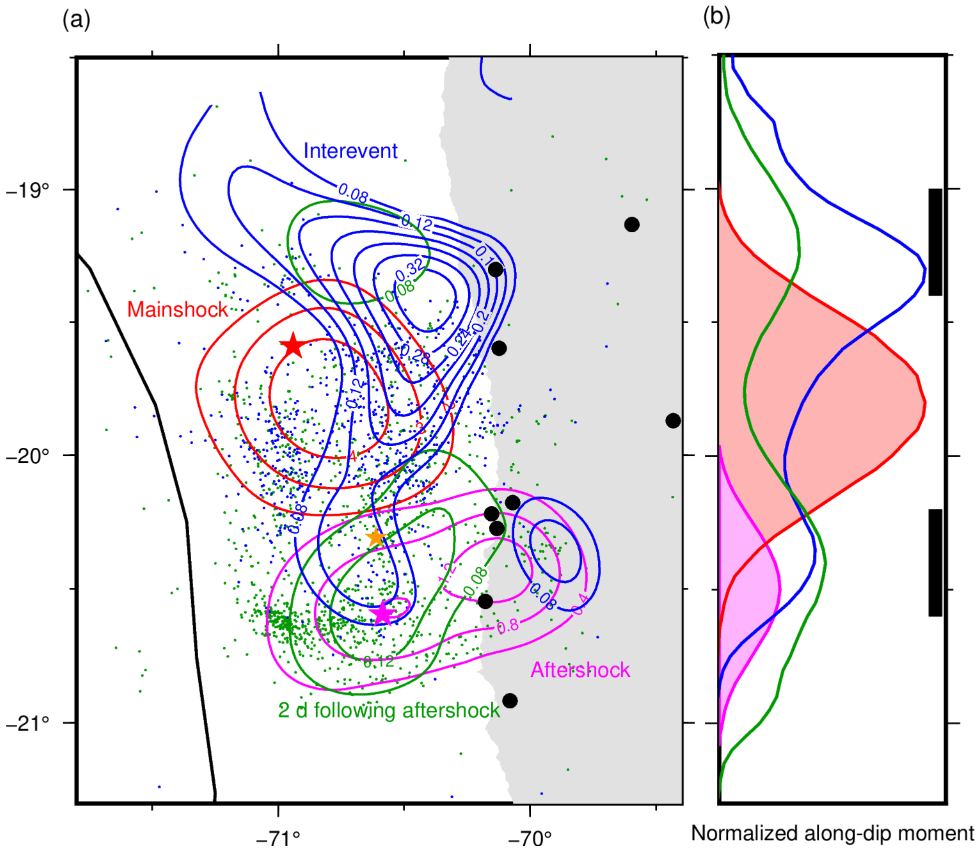

Figure 3. (a) Comparison of the slip at the four stages as labeled, inferred from displacements with the trajectory model fit (Figures 1b-e, S2a-c, and S10a-f). Blue and green dots are moderate seismicity during the corresponding stages in color (McBrearty et al., 2019). See Figure 1 for other elements. (b) Normalized along-dip moment of each stage (colors in (a)). Coseismic (red and magenta) and substantially aseismic (blue and green) moments are separately normalized with respect to their maximum values (ratio of the two normalizing factors is ~0.056). Two black bars indicate the inferred aseismic barrier locations.

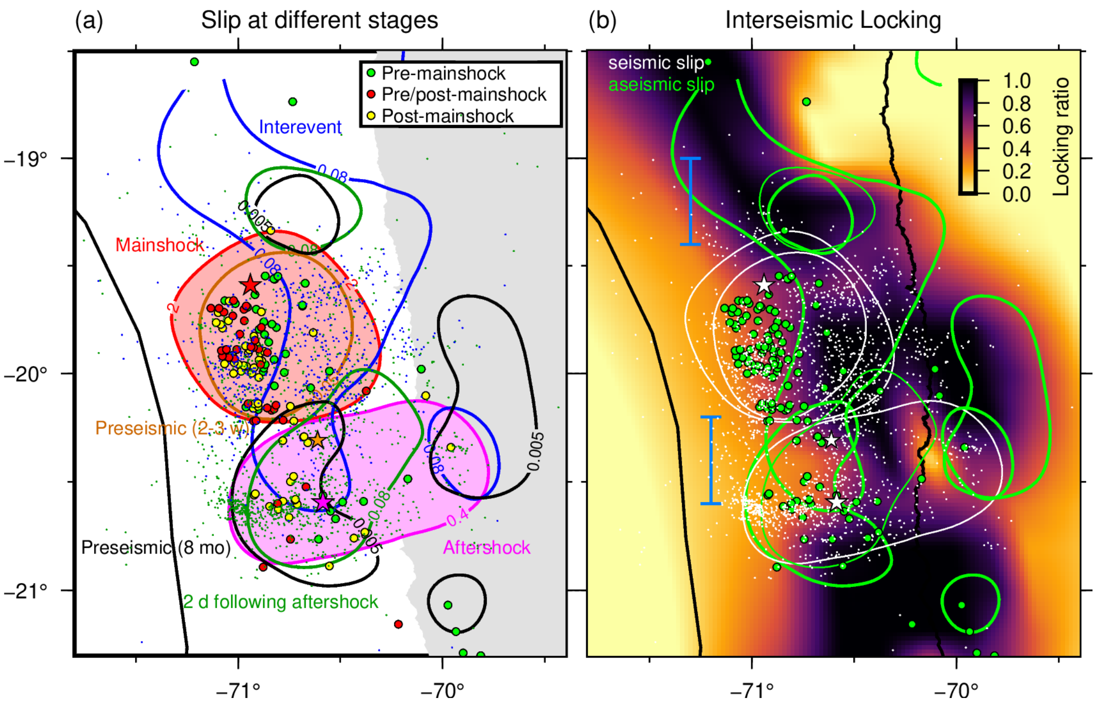

Figure 4. (a) Compilation of slips at different stages as labeled (this study and Socquet et al., 2017). Larger dots are repeaters (Meng et al., 2015). (b) Same as (a) but with interseismic locking (Métois et al., 2016) and seismic (white) and aseismic (green) slip events. Preseismic (2 – 3 weeks) slip is drawn as seismic slip because ~65% of moment release was released seismically (Socquet et al., 2017). Latitudinal range of inferred aseismic barriers is shown with two light blue bars. See Figure 3 for other elements.

Geophysical Research Letters

Supporting Information for

Largest aftershock nucleation driven by afterslip during the 2014 Iquique sequence

Yuji Itoh[1,2], Anne Socquet[1], and Mathilde Radiguet[1]

[1]Univ. Grenoble Alpes, Univ. Savoie Mont Blanc, CNRS, IRD, Univ. Gustave Eiffel, ISTerre, 38000 Grenoble, France.

[2]Earthquake Research Institute, The University of Tokyo, Tokyo, Japan.

Contents of this file

Text S1 to S4
Table S1
Figures S1 to S24

Text S1. Details of GPS data cleaning

We employed 5-minute high-rate GPS coordinates processed by Nevada Geodetic Laboratory (NGL; Blewitt et al., 2018). These coordinates are estimated by a Kalman filter and smoother with a random walk parameter of 17 m over the 5-minute interval (Blewitt et al., 2018; http://geodesy.unr.edu/gps/ngl.acn.txt and http://geodesy.unr.edu/gps_timeseries/QA.pdf; last accessed on 01 September 2023). Hence, forward and backward propagation of the rapid position changes due to the mainshock and the largest aftershock to the interevent and the post-largest-aftershock stages should be minimal. Also, NGL processes 5-min coordinates during each day individually and there is no additional smoothing or other treatment applied to coordinates near each day boundary (Blewitt et al., 2018). The mainshock and the largest aftershock occurred at 23:46:45.72UTC on 1 Apr 2014 and 02:43:13.94UTC on 3 Apr 2014, respectively (Soto et al., 2019a), so coordinates during 24 hours of the 27-hour interevent stage are individually processed and hence are free from the offsets of the two earthquakes. Therefore, we concluded that the interevent deformation found in this study is not a technical artifact of GPS processing.

We removed spatiotemporally correlated fluctuations in 5-minute coordinates processed through the following procedure. First, we fixed the GPS coordinates into the South American plate using a plate motion model with respect to ITRF2014 (Altamimi et al., 2007) (black in Figure S1). Then, we removed coordinate fluctuations due to multipath (e.g., Bock et al., 2000; Itoh & Aoki, 2022; Ragheb et al., 2007). Multipath signals are known to appear periodically, so we estimated them using Seasonal-Trend decomposition using LOESS (STL) (Cleveland et al., 1990; Pedregosa et al., 2011) which decomposes time series into trend, periodic (termed seasonal in the program), and residual terms. Here, we chose 86100 seconds (23 hours 55 minutes) for the period because it is the integer multiple of the sampling interval closest to the typical multipath period (86154 seconds or 23 hours 55 minutes 54 seconds; Ragheb et al., 2007). We removed the estimated periodic component and kept the other two terms for the subsequent analysis (red in Figure S1). Next, we removed diurnal variation in the data, using the same approach for the multipath removal but with a period of 86400 seconds (1 day; Itoh et al., 2022) (pink in Figure S1). Next, we removed common mode error which originates from the fluctuation of the reference frame and satellite orbit errors (Wdowinski et al., 1997), which is estimated in the following procedure.

We extracted common mode error by stacking time series at 6 sites in the nodal direction of the mainshock and aftershock, where little coseismic deformation is expected (Figure 1 and orange in Figure S1). Before stacking them, the time series at these sites went through the same noise removal procedure elaborated above and then we further removed outliers and a linear trend of time series at each site. The outliers are defined as epochs satisfying the following criterion (Equation (S1)) (Itoh et al., 2022);

$$\left|u_i - \frac{q_1+q_3}{2}\right| > n * \frac{q_3-q_1}{2} \quad \text{(S1)}$$

where, u_i is the displacement at the i-th epoch, q_1 and q_3 are the 25 and 75 percentile values of the position time series, respectively, derived from data between 60 days before and 30 days after the day of the mainshock. The term n is a threshold controlling how strict or loose we impose the outlier criterion and we adopted n = 8 in this study based on trial-and-error approaches. We estimated and removed the linear trend from the data after this outlier removal step.

Text S2. The trajectory model fit procedure and error evaluation of retrieved displacements

We retrieved surface deformation at the four stages from the following trajectory model fit result with Equation (S2) (Figures 1b-e, S2a-d, and S8a-f).

$$x(t) = a + \left\{b + c\log\left(1 + \frac{t-t_0}{d}\right)\right\}H(t-t_0) + \left\{e + f\log\left(1 + \frac{t-t_1}{g}\right)\right\}H(t-t_1) \quad \text{(S2)}$$

where *a, b,* and *e* are the initial position and coseismic offsets of the mainshock (at time $t = t_0$) and the largest aftershock (at $t = t_1$), respectively. The first and second logarithmic terms model postseismic responses assuming velocity-strengthening afterslip (Marone et al., 1991; Perfettini & Avouac, 2004; Perfettini et al., 2018) induced by the mainshock and the largest aftershock, respectively. Different functions (Marill et al., 2021; Periollat et al., 2022) did not improve the fit. We determined the amplitude of each term by the least square regression. Coseismic displacements of the two quakes (Figures S10a-b, S10d-e, and S15) are from the step terms (i.e., b and e) while displacements during the two interevent and the post-largest-aftershock stages are increment of the model prediction for the time window of interest (Figures 1b, S2d, S8c, S8f, and S10-S11). The search range for d and g in Equation (S2) is 0.1 – 3 and 0.1 – 10 days, respectively (Figure S3). For sites north of 19°S, we excluded the term relating to the largest aftershock (i.e., the third term of Equation (S2)) and set the search range for d as 0.1 – 10 days by considering the largest aftershock size and the great hypocenter distance.

We applied this trajectory model to fit the cleaned time series twice to remove outliers. We used Equation (S1) in both of the two fitting steps, but, after the first fit, we removed outliers defined as epochs which deviate from the model prediction by 3 times post-fit RMS (Figure S4) because the time series of the sites in the main region of interest have not yet gone through the outlier removal using Equation (S2). RMS is here defined as

$$RMS = \sqrt{\frac{\sum_{i=1}^{n}\left(\frac{o(t_i)-x(t_i)}{w(t_i)}\right)^2}{\sum_{i=1}^{n}\frac{1}{w(t_i)^2}}} \quad \text{(S3)}$$

Where, $o(t_i)$ and $w(t_i)$ are a coordinate and its error at $t = t_i$, respectively and n is the number of available epochs. Then, we again fit the same function to the data without the outliers. We preferred to employ the classical 3*RMS criterion of Equation (S3) than Equation (S1) to define the outliers at the main sites of interest after obtaining the residual of the first fit because we carried out the least square trajectory model fit. However, we admit that there would be no strong superiority in our choice of Equation (S3) over Equation (S1).

For simplicity, formal displacement errors of the coseismic displacements are obtained by the linear least-square transformation of the GPS position observation errors while formal errors of the displacements during the two aseismic stages were defined as Equation (S3) but with the time windows of each stage.

Text S3. Details of the moving median analysis

We derived the moving median (Figures 2a-b) from the data after removing the mainshock and largest-aftershock coseismic steps determined by the trajectory model fit. We did not exclude the pre-mainshock or post-largest-aftershock coordinates for deriving moving median values the first or last 0.25 days because, given the definition of median, distortion of the obtained moving median should be limited. Using a shorter window length by excluding the pre-mainshock or post-largest-aftershock coordinates from the calculation ended up underestimating the rapid transient deformation at the very beginning of the interevent stage (Figure S22). We computed displacements during the two interevent substages and the whole interevent stage by simply taking the difference of coordinates (Figures 2e-f and S17). For simplicity, their formal errors are taken from the trajectory analysis results (See Text S2).

Text S4. Inversions of incremental interevent displacements derived from the motogram analysis

For the interevent afterslip, we used four different datasets, namely, (i) the cumulative interevent displacements derived from the trajectory model fit (i.e., Equation (1); Figures 1b, 3a, and S2d-e), (ii) same as (i) but displacements derived from the moving median (Figures S17a-b), (iii) displacements during the first interevent substage, derived from the moving median (Figures 2e and S17c) and (iv) same as (iii) but during the second interevent substage (Figures 2f and S17d).

For inversions of the interevent afterslip with the datasets derived from the moving median analysis (i.e., Datasets (ii), (iii), and (iv); Figures 2e-f and S17), we excluded GPS sites located north of 19°S, namely those near the border of Chile and Peru, because including them highly destabilized the slip inversion (Figures S23-S24). Furthermore, to obtain the consistent slip pattern in all the interevent slip models, we added a constraint to the upper bound of the slip amplitude (Figures S23-S24). For the cumulative slip inversion with Dataset (ii), the upper bound is set to those obtained by the inversion of displacements obtained by the trajectory model fit (i.e., Dataset (i); Figure 3a). The obtained slip amplitude was subsequently used as the upper bound of slip amplitude (Figures S17a-b) during the first and second interevent substages with the datasets (iii) (Figures 2e and S17c) and (iv) (Figures 2f and S17d). For the reason of practical implementation, we did not require the sum of slip or moment at each subfault at the two substages to be equal to those derived from the whole period dataset (i) or (ii). The sum of the moments at the two substages is slightly smaller than the inversions at the whole period (Table S1; Figure S14).

Text S5. Coulomb stress change calculation

We computed coulomb stress change (CSC) associated with the mainshock and the interevent aftershock (Figure S9). CSC is defined as follows.

$$CSC = \Delta\tau + \mu\Delta\sigma \quad (4)$$

where, $\Delta\tau$ and $\Delta\sigma$ indicate elastic shear and normal stress change induced by slip, respectively. Positive $\Delta\tau$ is taken in a hypothetical slip direction of receiver fault defined as the convergence direction of Nazca and South American plates. Positive $\Delta\sigma$ is taken in an unclamping direction. The term μ is a static effective frictional coefficient which was set to 0.4.

Table S1. Geodetic, seismic, and aseismic moments and equivalent moment magnitude (N m / M_w) evaluated in this study at the interevent stage.

	Interevent total [c]	Interevent total [d]	1st substage [e]	2nd substage [f]
The entire model region				
Geodetic	$9.0*10^{19}$ / 7.2	$7.9*10^{19}$ / 7.2	$5.7*10^{19}$ / 7.1	$1.5*10^{19}$ / 6.7
Seismic[a]	$2.4*10^{18}$ / 6.2	Same as left	$5.4*10^{17}$ / 5.8	$1.8*10^{18}$ / 6.1
Aseismic[b]	$8.9*10^{19}$ / 7.2	$7.8*10^{19}$ / 7.2	$5.6*10^{19}$ / 7.1	$1.4*10^{19}$ / 6.7
The mainshock latitude (referred to as "North")				
Geodetic	$7.2*10^{19}$ / 7.2	$6.3*10^{19}$ / 7.1	$4.6*10^{19}$ / 7.0	$1.1*10^{19}$ / 6.6
Seismic[a]	$5.2*10^{17}$ / 5.7	Same as left	$4.8*10^{17}$ / 5.7	$4.1*10^{16}$ / 5.0
Aseismic[b]	$7.1*10^{19}$ / 7.2	$6.3*10^{19}$ / 7.1	$4.5*10^{19}$ / 7.0	$1.1*10^{19}$ / 6.6
The largest aftershock latitude (referred to as "South")				
Geodetic	$1.8*10^{19}$ / 6.8	$1.6*10^{19}$ / 6.7	$1.1*10^{19}$ / 6.6	$4.8*10^{18}$ / 6.4
Seismic[a]	$1.8*10^{18}$ / 5.7	Same as left	$5.9*10^{16}$ / 5.1	$1.8*10^{18}$ / 6.1
Aseismic[b]	$1.6*10^{19}$ / 6.7	$1.6*10^{19}$ / 6.7	$1.1*10^{19}$ / 6.6	$3.1*10^{18}$/ 6.3

[a] Determined by the seismicity analysis with a magnitude of the event 45 minutes before the largest aftershock fixed
[b] Geodetic – Seismic
[c] Geodetic moment determined by the slip inversions of GPS data (dataset (i); Text S4)
[d] Geodetic moment determined by the slip inversions of GPS data (dataset (ii); Text S4)
[e] Geodetic moment determined by the slip inversions of GPS data (dataset (iii); Text S4)
[f] Geodetic moment determined by the slip inversions of GPS data (dataset (iv); Text S4)

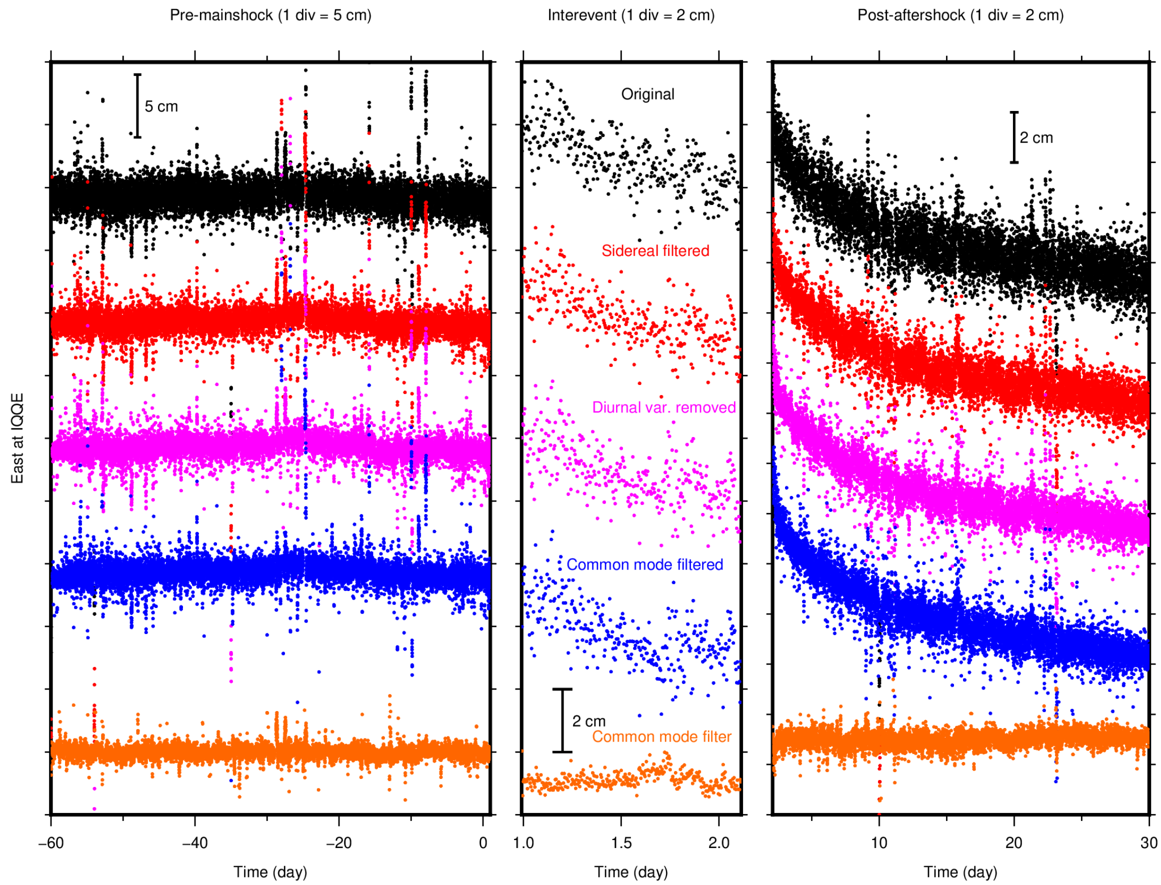

Figure S1. High-rate 5-min GPS data cleaning procedure (East component at IQQE as an example; Figure 1d). Time series with each color indicates the results of the cleaning procedure at each step as labeled. Coseismic steps of the mainshock and the largest aftershock are removed by breaking panels.

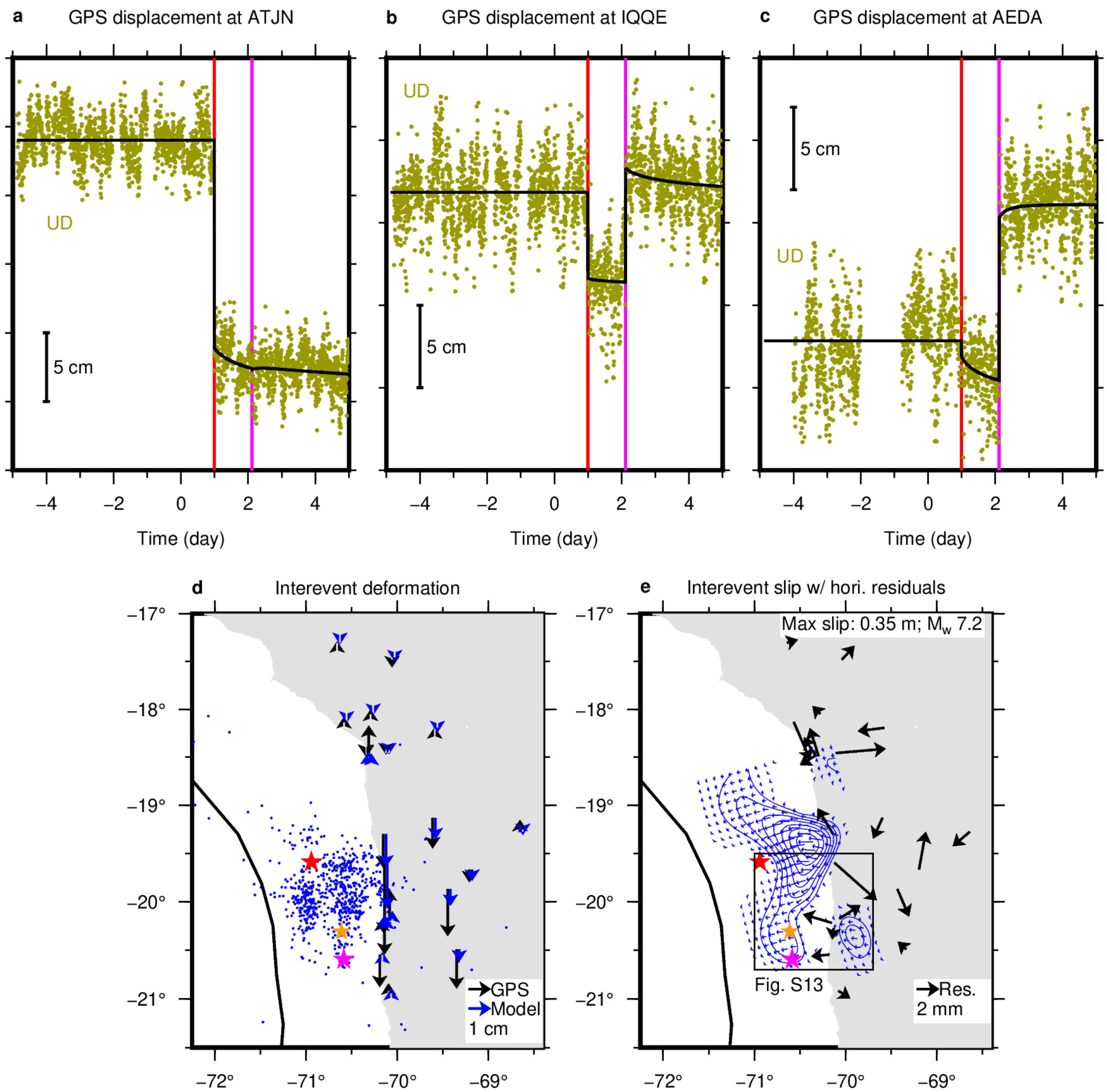

Figure S2. Data analysis and slip inversion result using the trajectory function fit approach. (a) – (c), Trajectory model fit results for vertical components at three sites as labeled. Location of these sites is shown in Figure 1b. (d) Vertical interevent GPS displacements (black vectors) together with model prediction (blue vectors) from aseismic slip inversion shown in (e) and Figure 2a. Refer to Figure 3 for other elements. (e) The inferred interevent slip (blue contours) with normalized slip vectors. Black vectors indicate horizontal residuals of the inversion (GPS – Model in Figure 1b).

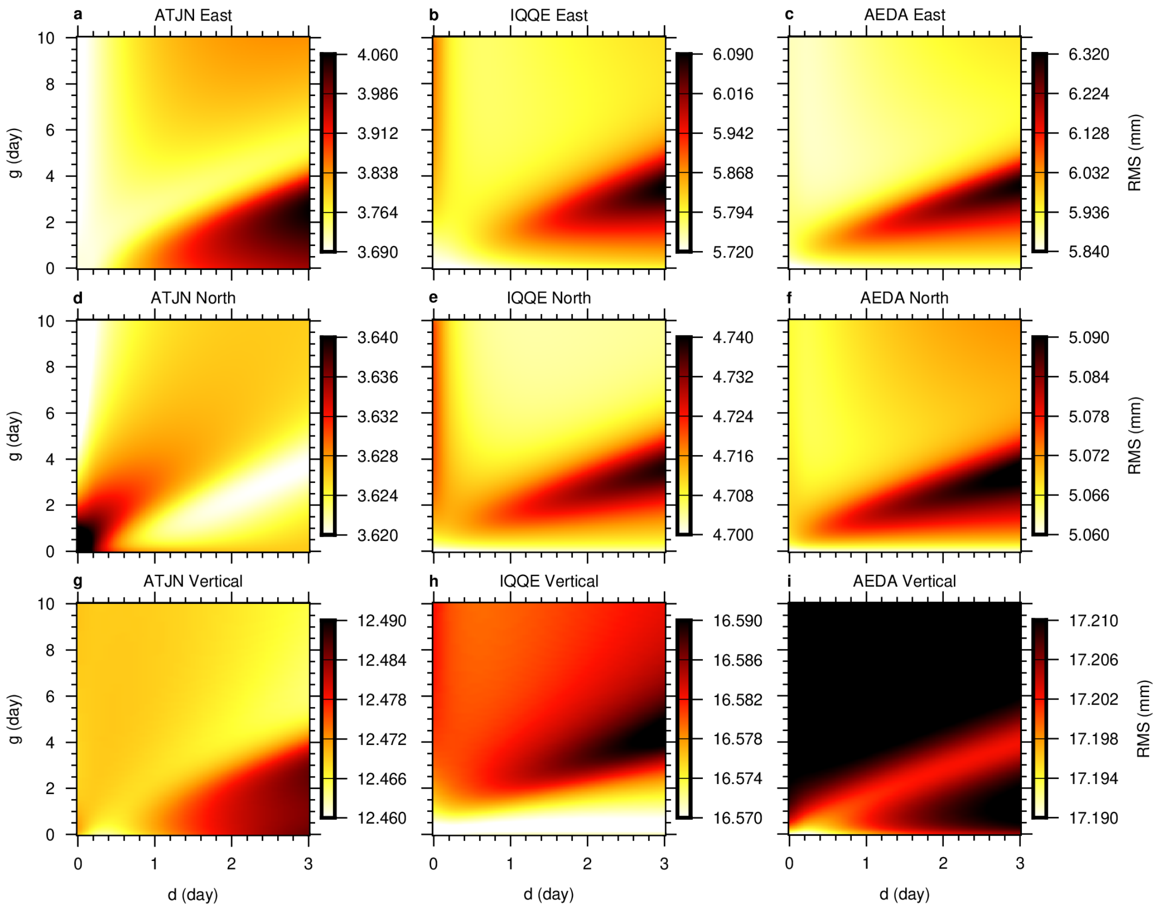

Figure S3. Distribution of RMS of the trajectory model fit with respect to different d and g in Equation (S2) (color). (a-c), Results for the east component at three sites as labeled. Site location is shown in Figure 1b. (d-f) and (g-i) Same as (a) – (c) but for the north and the vertical components, respectively.

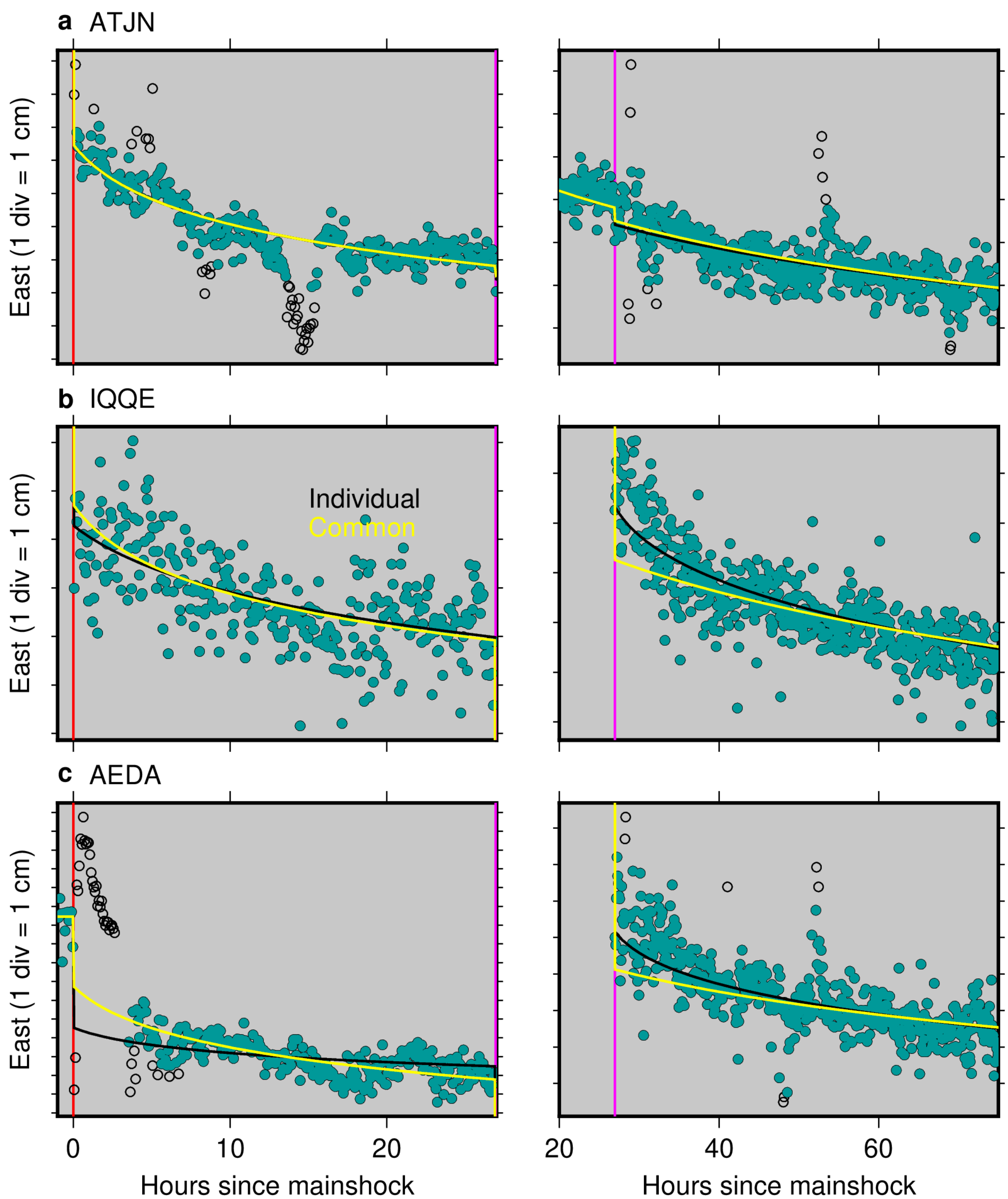

Figure S4. Comparison of trajectory model fit results with individual (black) and common (yellow) time constant values *d* and *g* (Equation (S2)) for all the sites and components at selected sites as labelled (locations in Figure 1b). Only the zoom-in around the mainshock and the largest aftershock time (indicated by vertical lines in red and magenta) are shown. Green and open dots indicate coordinates remained and removed by the outlier removal step after the first fit (See Text S2 for details).

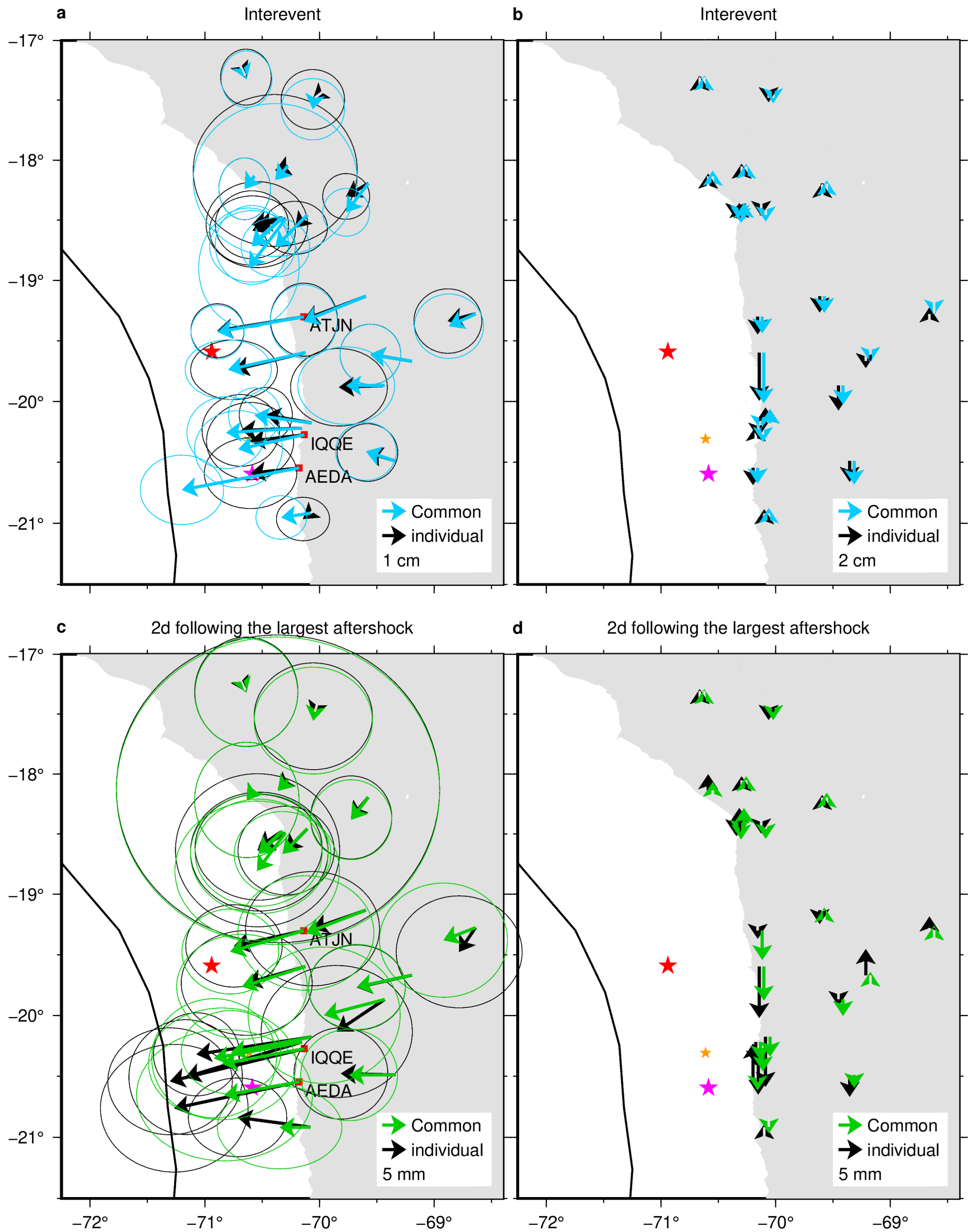

Figure S5. Comparison of cumulative displacements at the interevent (a: horizontal; b: vertical) and the post-largest aftershock (c: horizontal; d: vertical) stages retrieved from the trajectory model with common (light blue or green) and individual (black) time constant values *d* and *g* (Equation (S2)) for all the sites and components. The error ellipses for the vertical components are trimmed for visual clarity. Refer to Figure 1b for other elements

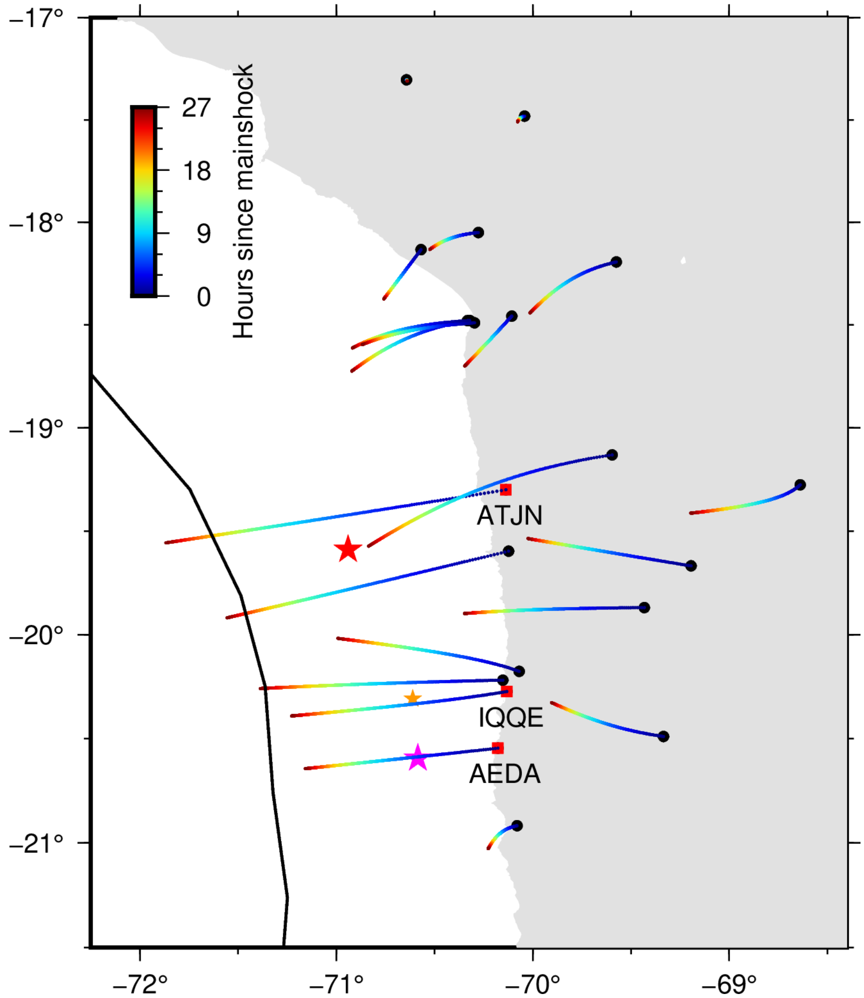

Figure S6. Interevent GPS site motion inferred from the trajectory model (Equation (S2)) drawn as motograms. The original time series at the three selected sites (red squares with site names) are shown in Figures 1c-e and 2b.

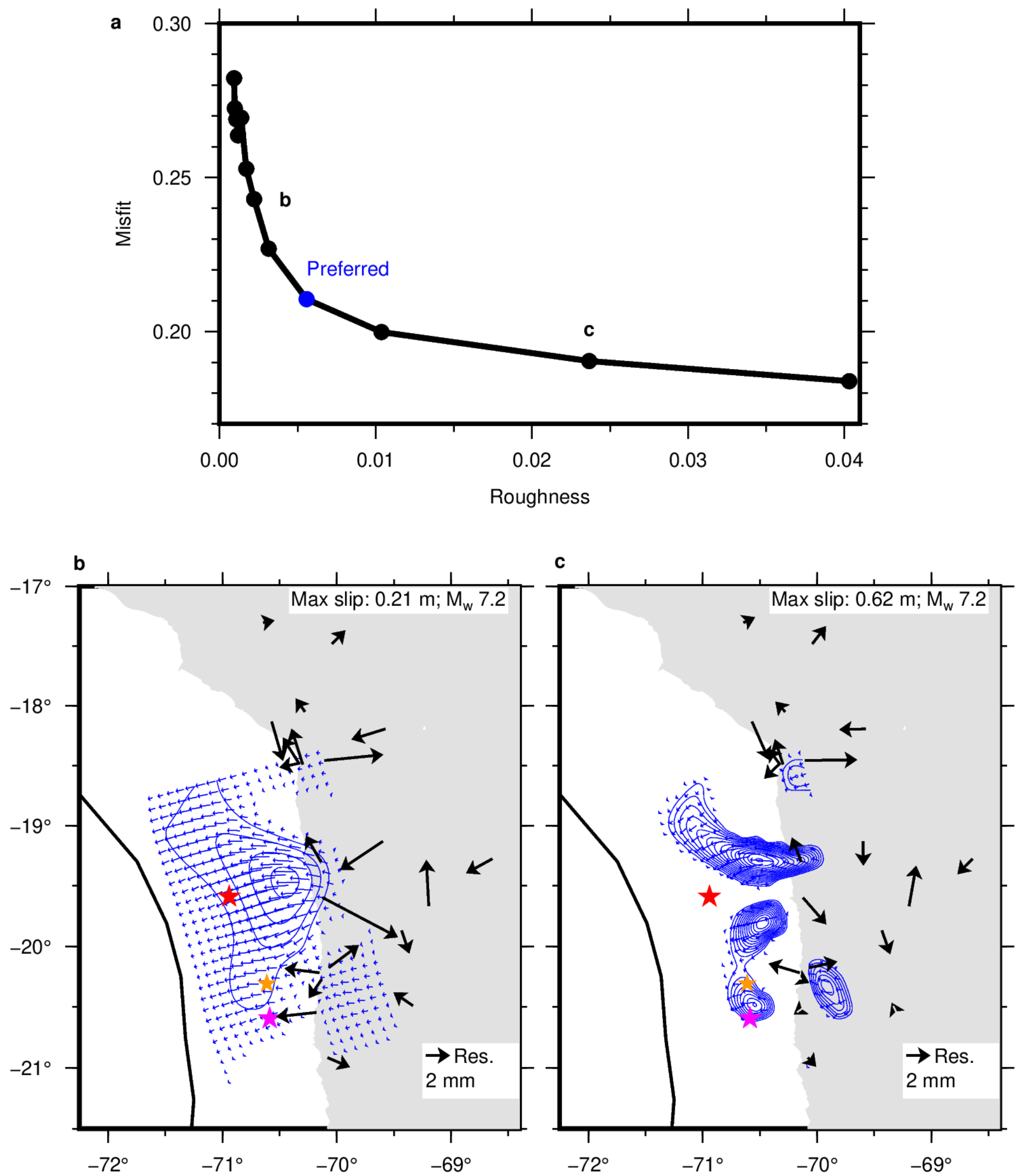

Figure S7. Trade-off curve of the slip roughness and misfit and model variations for the interevent slip inversion using the displacements derived from the trajectory model fit. (a) Trade-off curve. Dots indicate preferred (blue) and other tested models. (b-c), model variation with different slip roughness as shown in (a). Refer to Figure S2e for other elements.

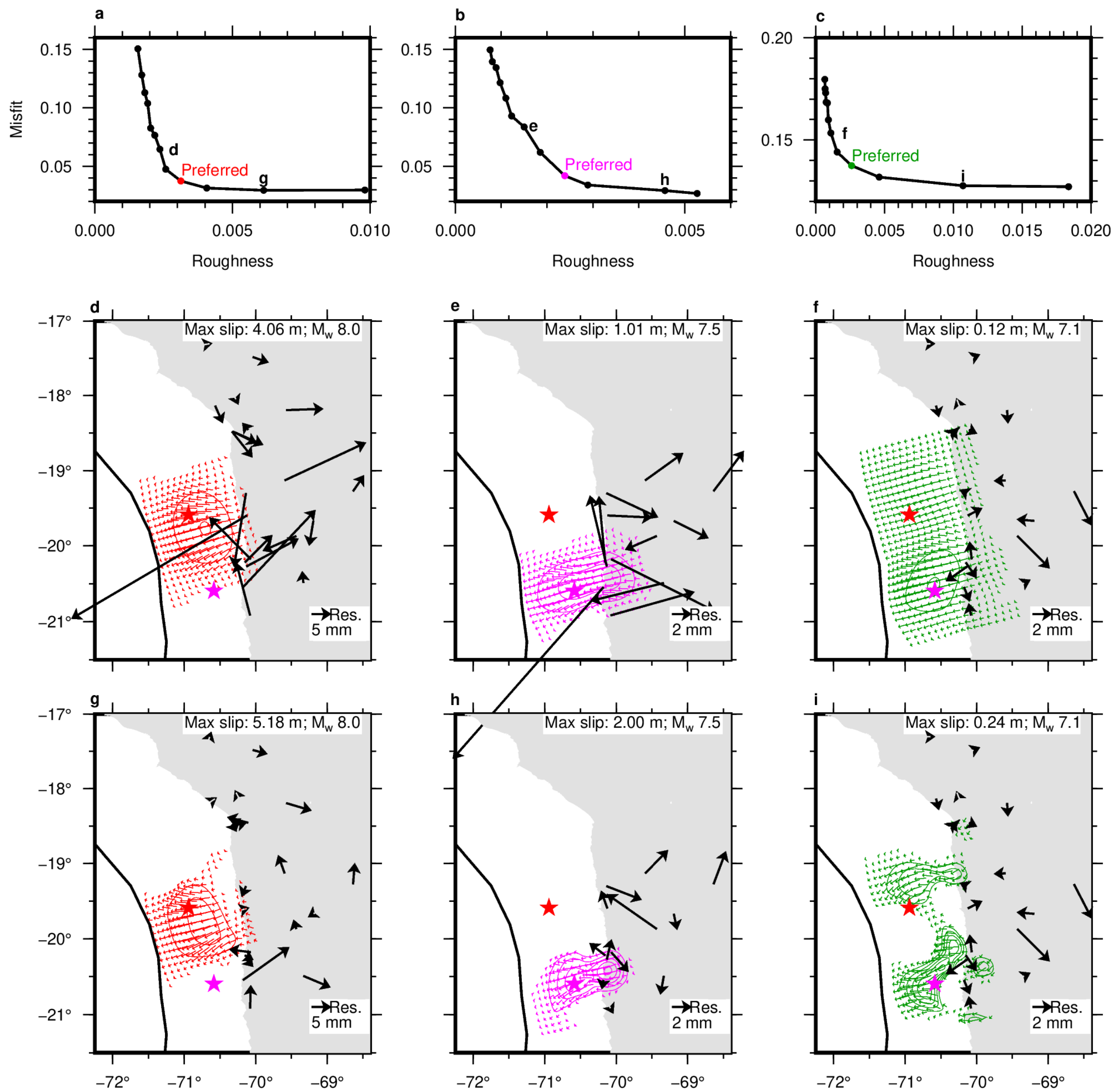

Figure S8. Trade-off curve of the slip roughness and misfit and model variations for the mainshock, the largest aftershock, and the post-largest-aftershock 2-day slip. (a-c) Trade-off curve for the mainshock (a), the largest aftershock (b), and subsequent 2-day afterslip (c). Dots indicate preferred (red, magenta, or green) and other tested models. (d-i) model variation with different slip roughness as shown in (a) – (c). Refer to Figures S15g-i for other elements.

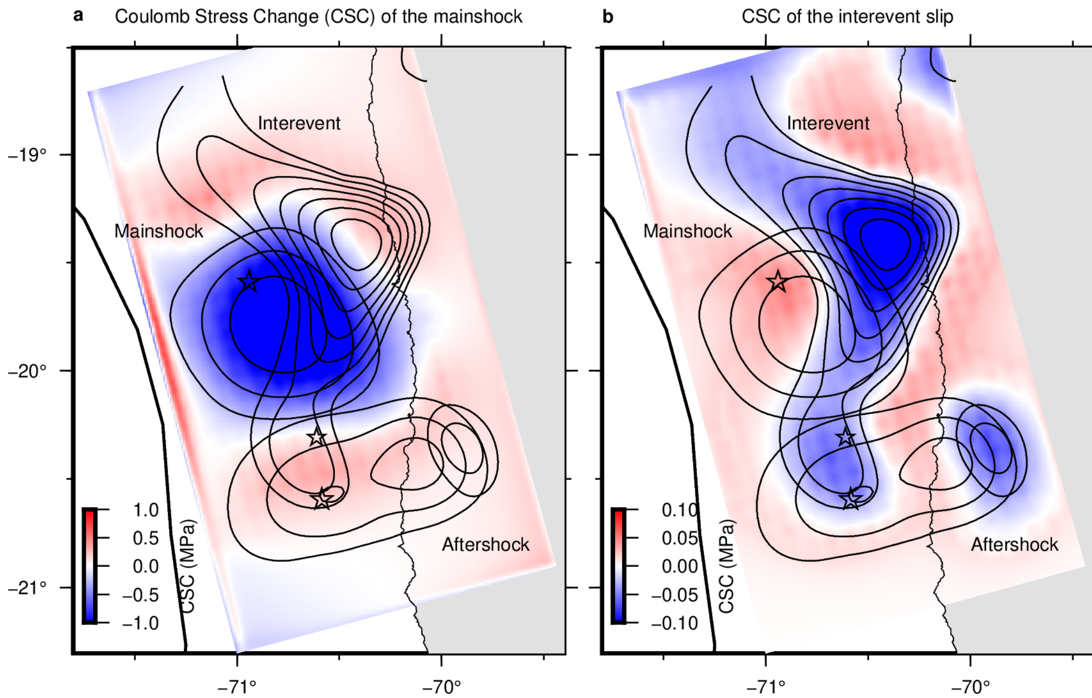

Figure S9. Coulomb stress change (CSC) associated with the mainshock (a) and the interevent slip (b). Solid contours are slip distribution of the mainshock, the interevent slip, and the largest aftershock, as labeled. Refer to Figure 3 for contour interval and open stars.

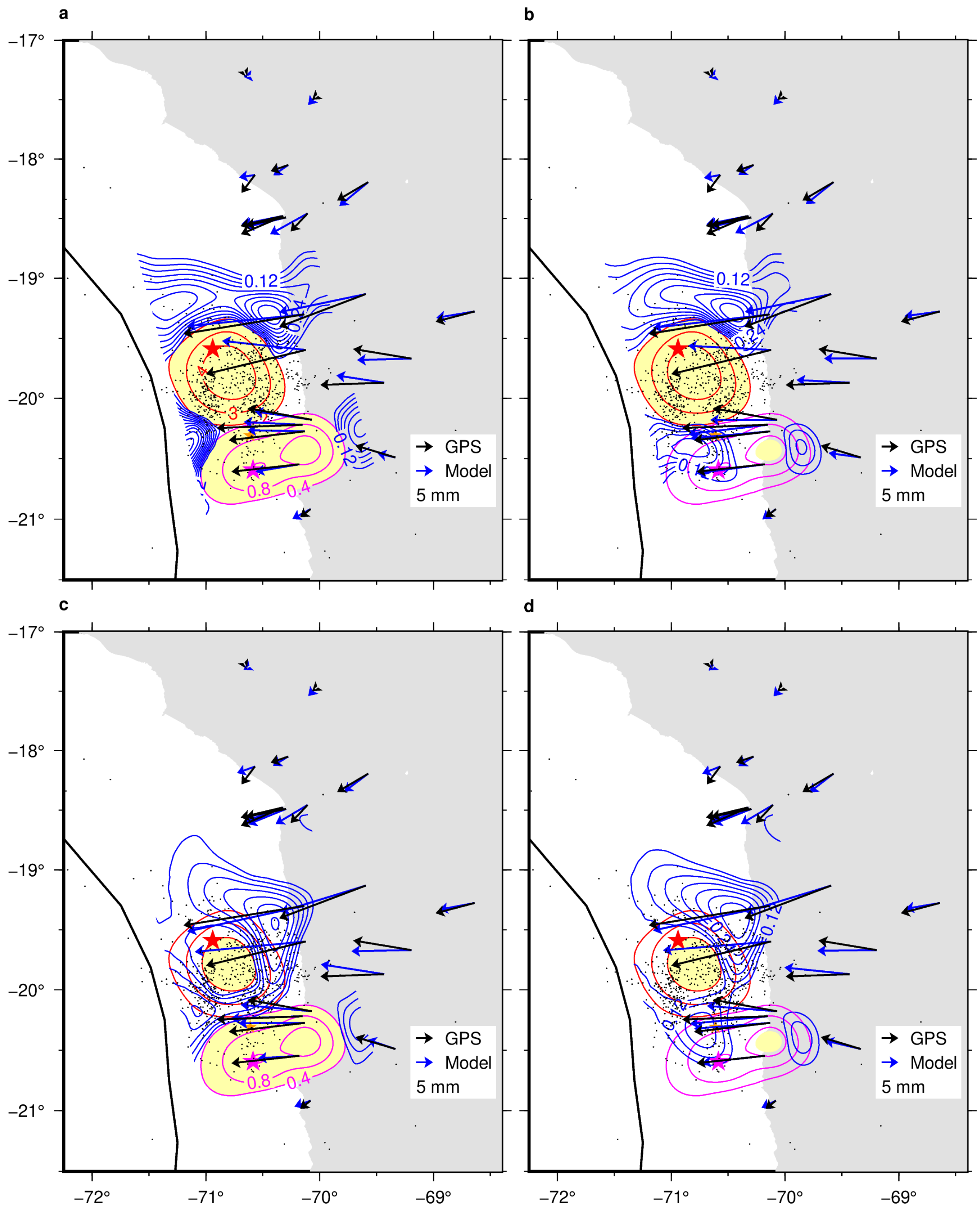

Figure S10. Results of interevent slip inversions (blue contours) with part of the seismic slip regions forced to have zero-slip (yellow). Black does are the interevent seismicity (McBrearty et al., 2019). Refer to Figures 1b and 3 for other elements.

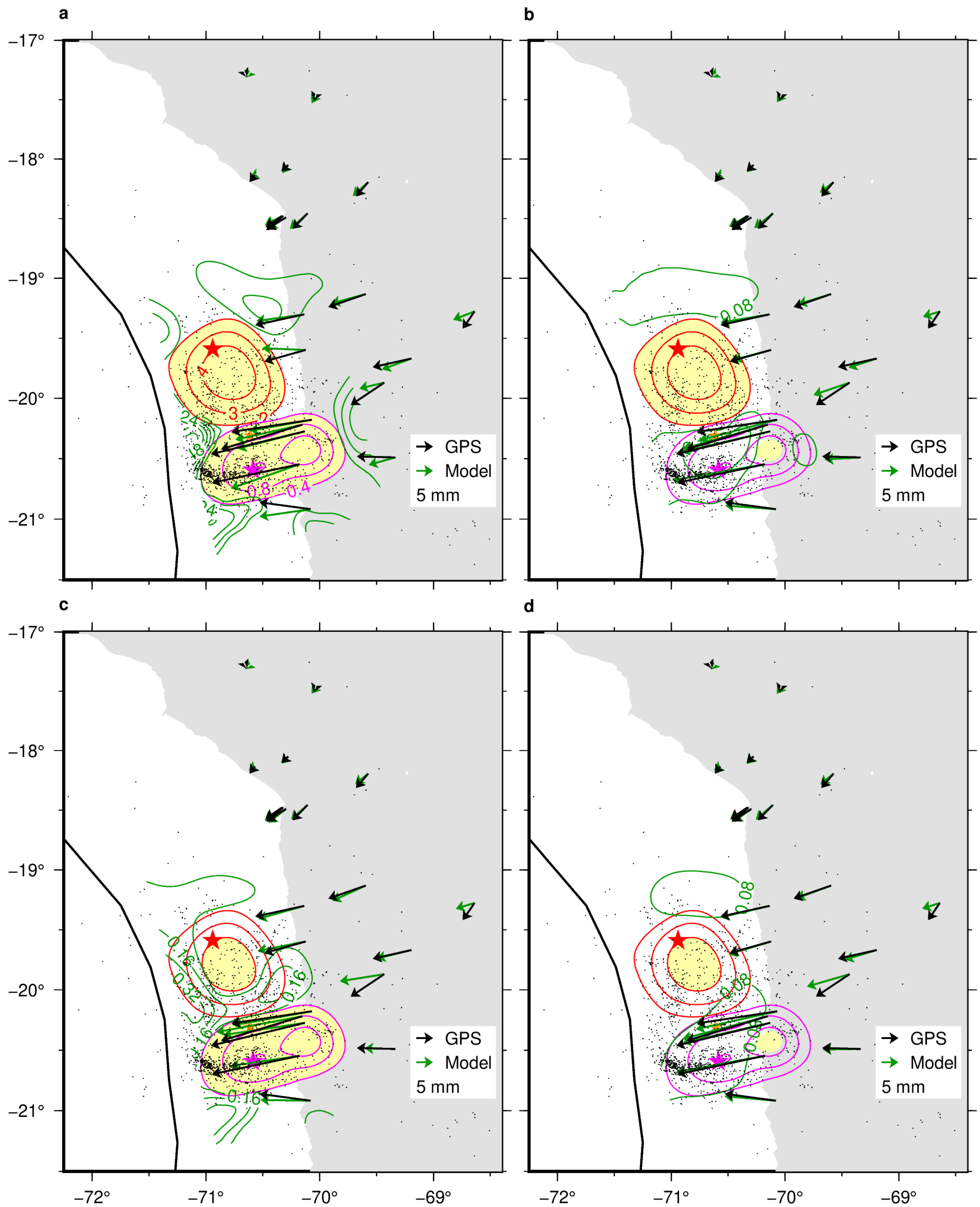

Figure S11. Same as Figure S10 but for the post-largest-aftershock slip for 2 days drawn in green. The black dots are the post-largest-aftershock seismicity for the 2 days. Refer to Figures 2c and 3 for other elements.

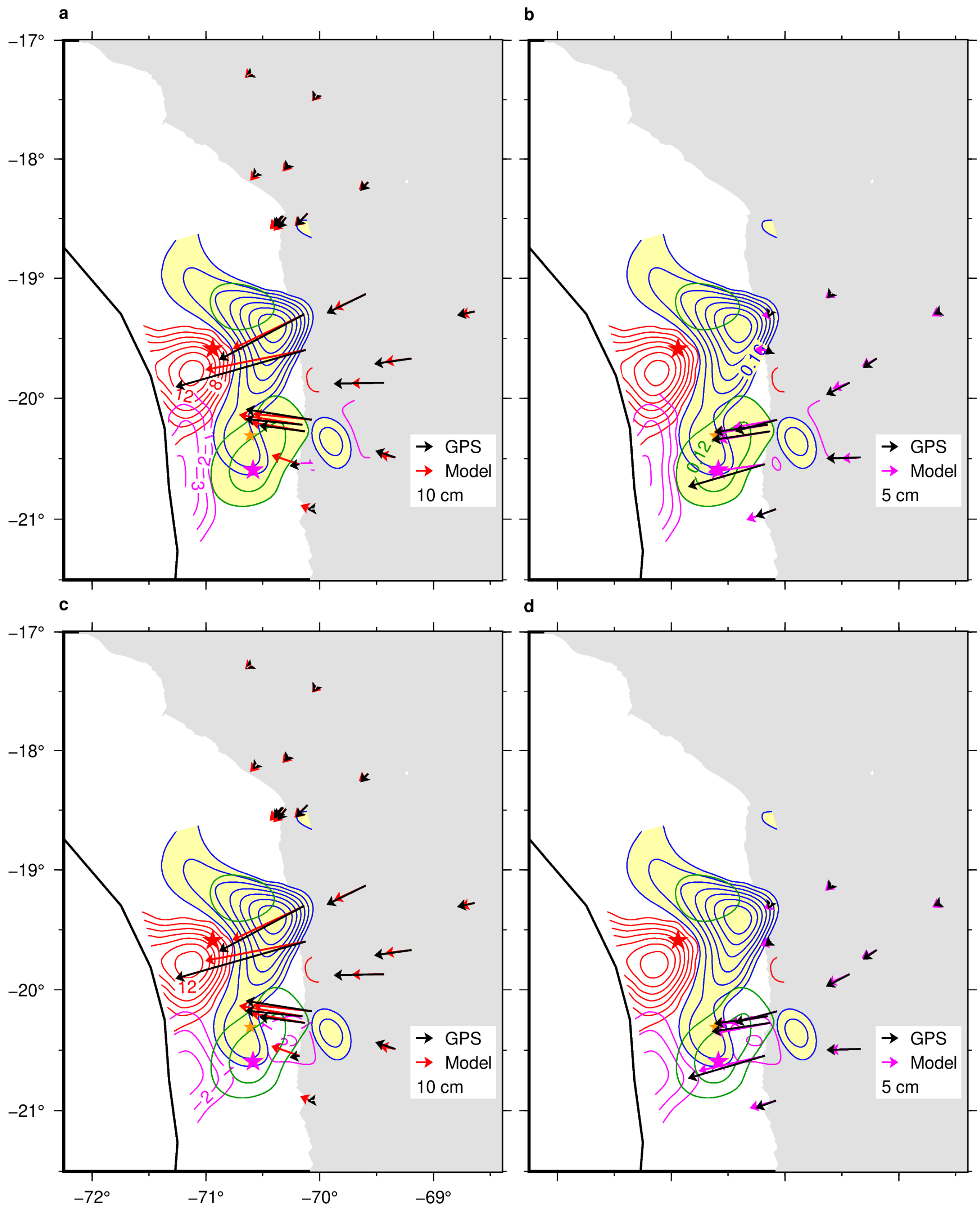

Figure S12. Results of coseismic slip inversions (red and magenta contours for the mainshock and the largest aftershock, respectively) with part of the interevent and post-largest-aftershock slip regions forced to have zero-slip (yellow). Refer to Figures 2a-b and 3 for other elements.

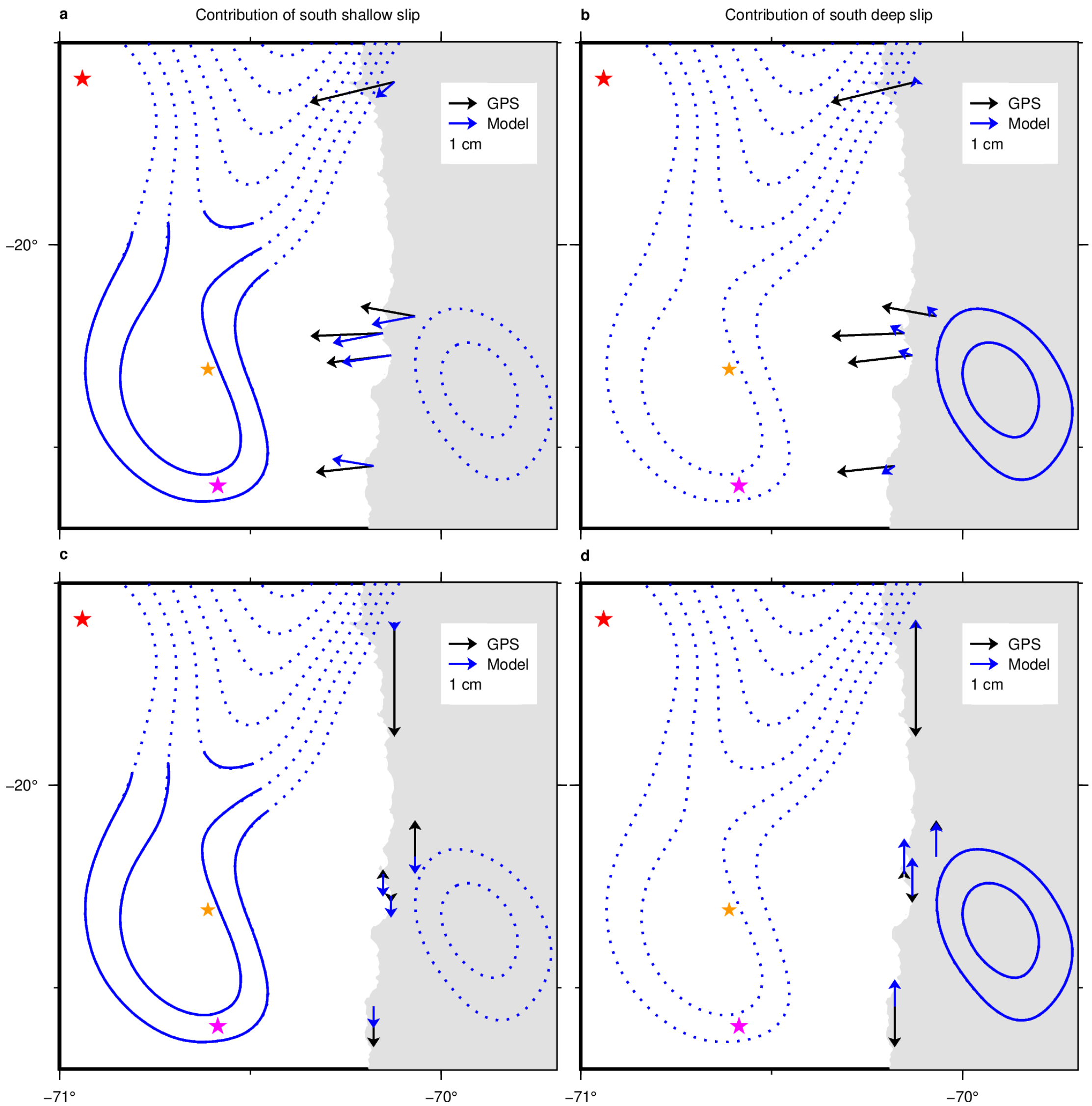

Figure S13. Forward modeling test results for the interevent slip. Comparison of interevent GPS displacements derived from the trajectory model fit (black) and model prediction (blue) computed from a subset (solid contours) of interevent slip inferred from the black vectors (solid + dot contours). (a-b), Comparison of horizontal displacements. (c-d) Same as (a) – (b) but for vertical displacements. Refer to Figure S2e to identify the plot area.

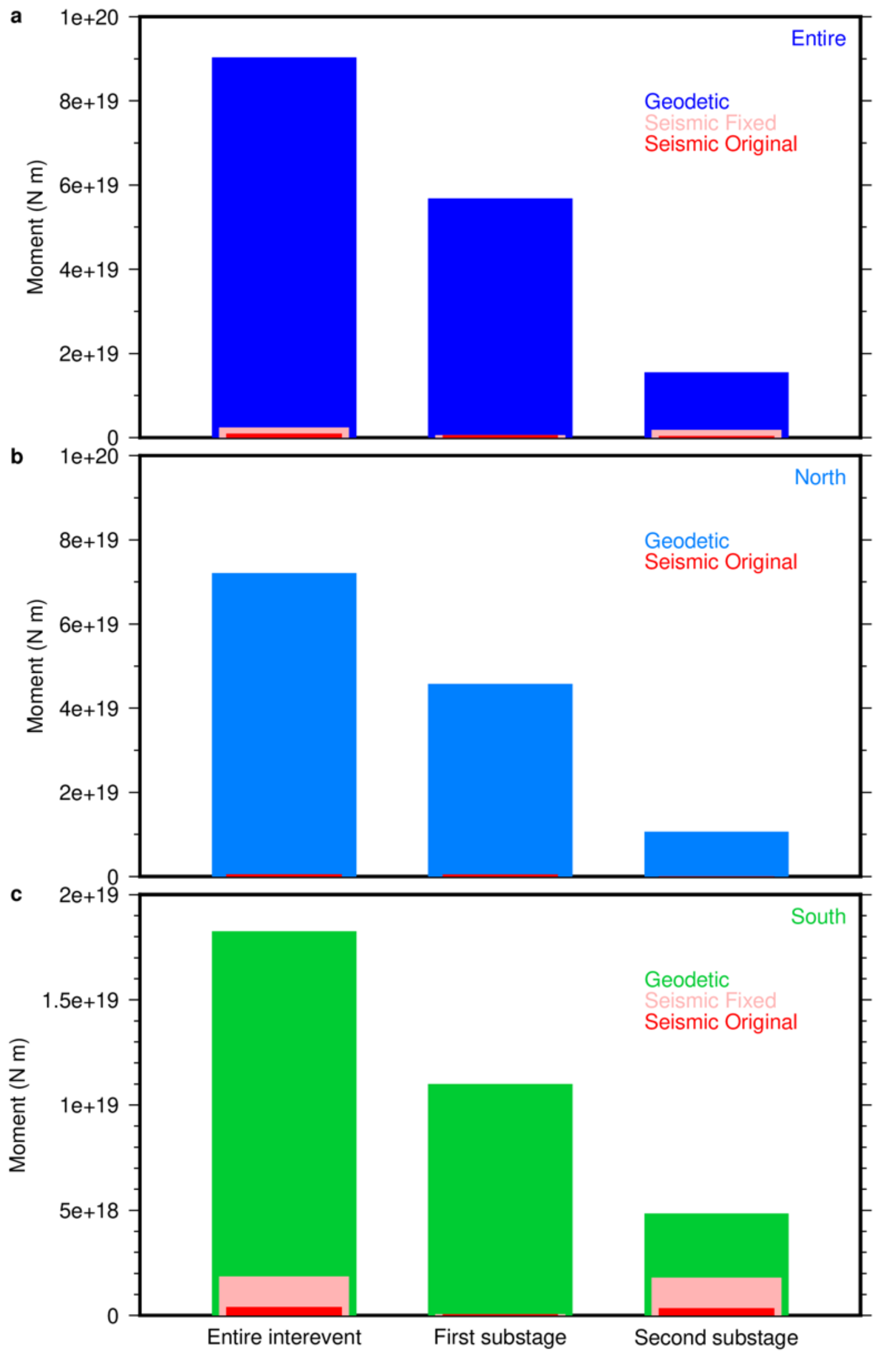

Figure S14. Comparison of geodetic and seismic moments during the entire interevent stage and the first and second substages as labeled in the entire (a) region and the north (b) and south (c) subregions (Table S1). The top of each bar with different colors indicates a corresponding moment value. “Seismic Fixed” means that the magnitude of the “M 6.1” event, described as M 5.6 in McBrearty et al. (2019) is fixed to M_w 6.1 when calculating the seismic moment (See Main text) while “Seismic Original” is not. Geodetic moments of the entire interevent period (left) are taken from the first left column of Table S1.

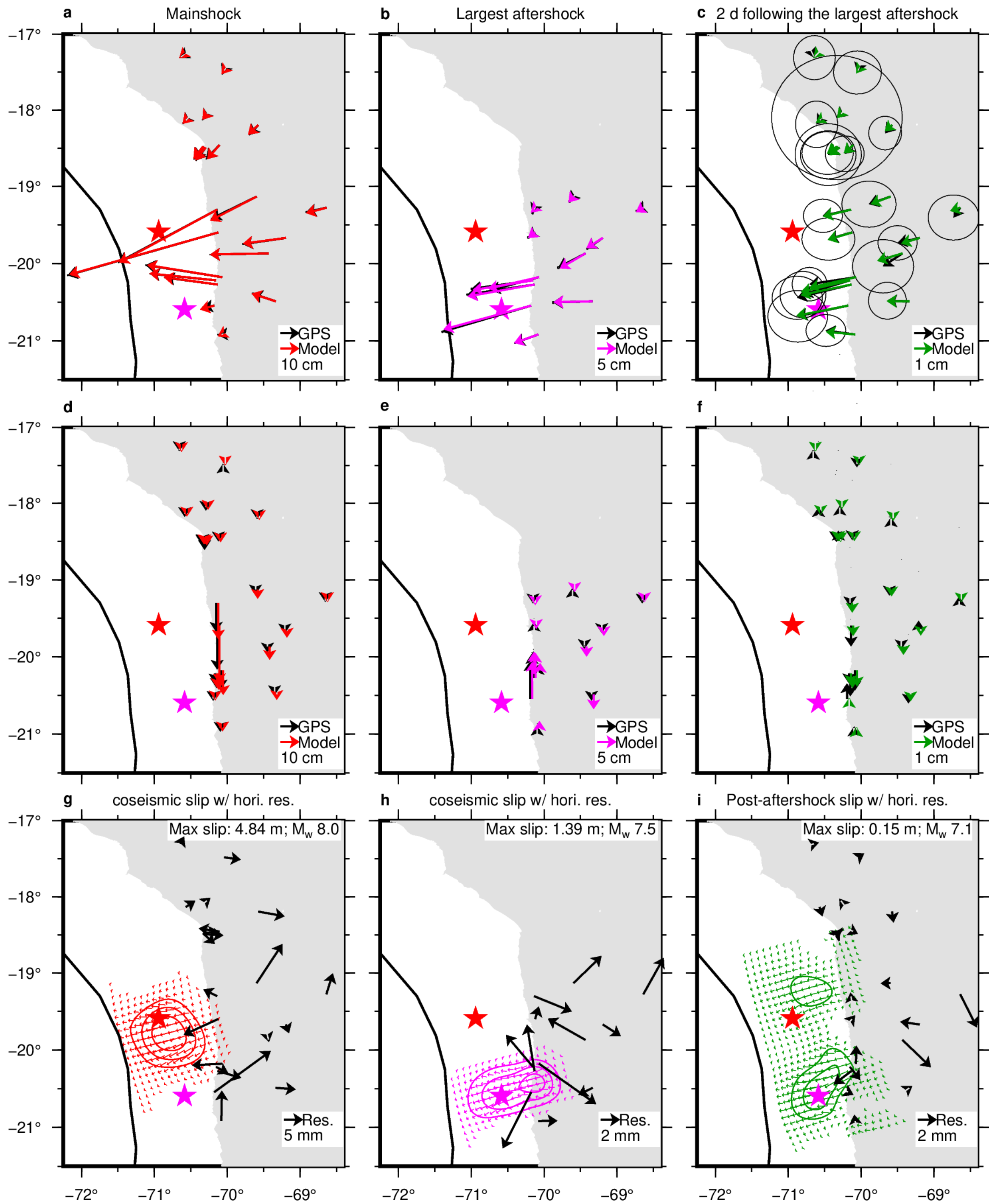

Figure S15. Data analysis and inversion results for the mainshock (a, d, and g), the largest aftershock (b, e, and h), and the post-largest-aftershock stage (2 days; c, f, and i). (a-c), Horizontal GPS displacements at each stage derived from the trajectory model fit. (d-f), Same as (a) – (c) but for vertical displacements. (g-i), Slip inversion results (contours) at each stage with normalized slip vectors. Black vectors indicate horizontal residuals of the inversion (GPS – Model).

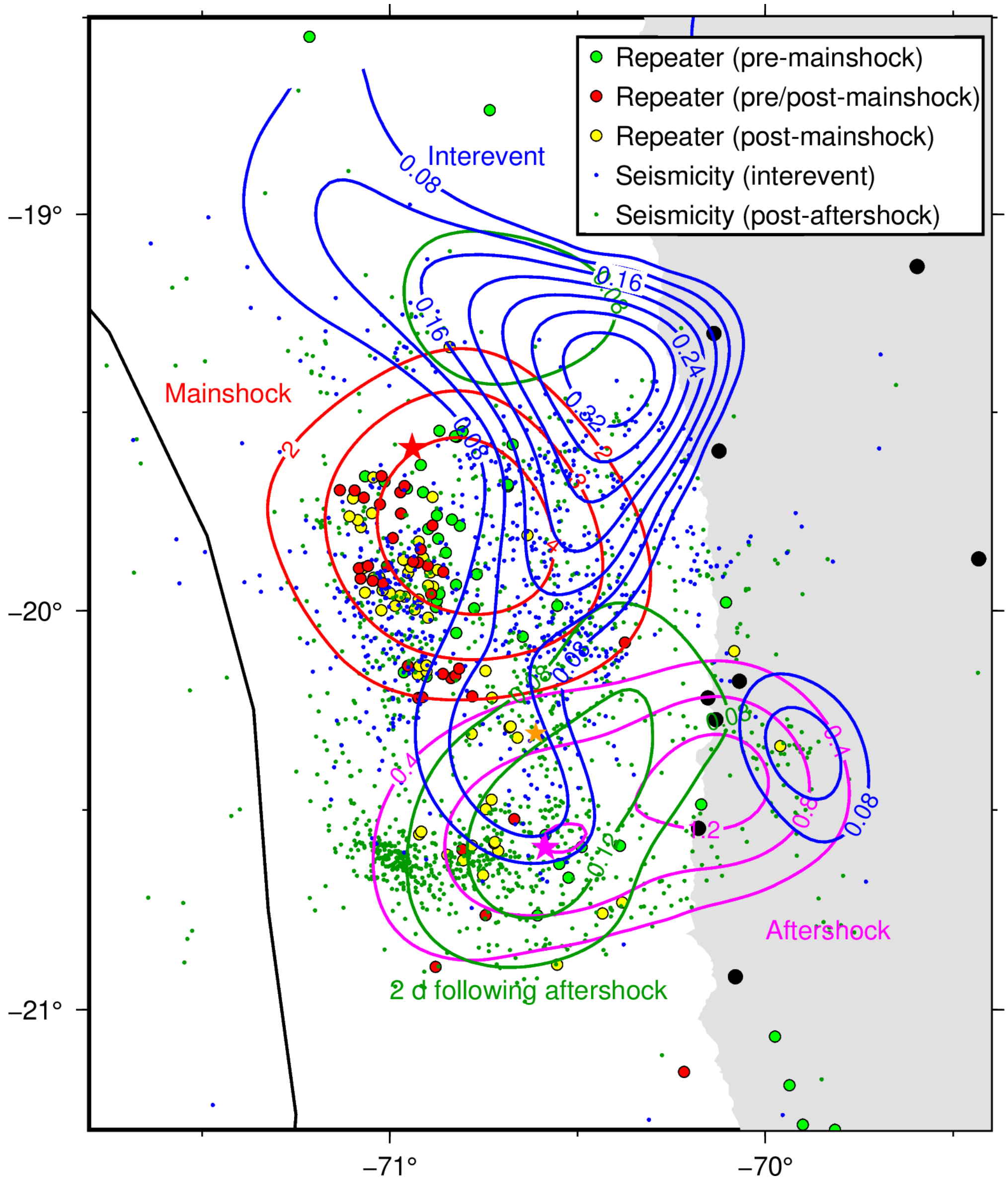

Figure S16. Same as Figure 3a but with the repeaters of Meng et al. (2015; Figure 4a) as labeled.

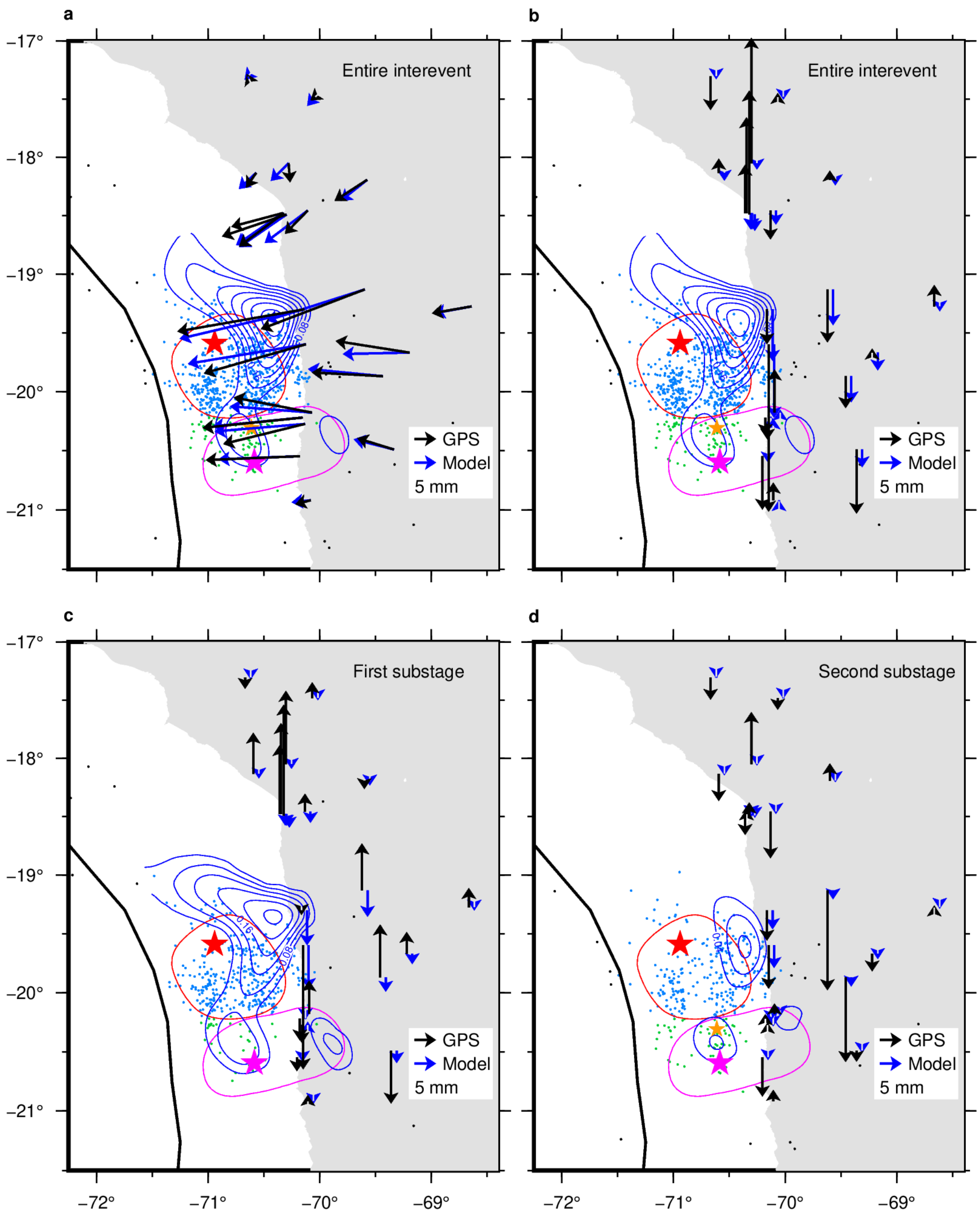

Figure S17. Data analysis and slip inversion result using the moving median approach. (a-b) Cumulative interevent horizontal (a) and vertical (b) displacements (black vectors) derived from the moving median analysis, together with the model prediction (blue vectors) from the inferred slip (blue contours). Refer to Figure 2 for other elements. Note that GPS displacements at sites north of 19°S are not inverted. (c-d) Same as Figures 2e-f but with vertical GPS displacements derived from the moving median analysis (black vectors) and model predictions (blue vectors).

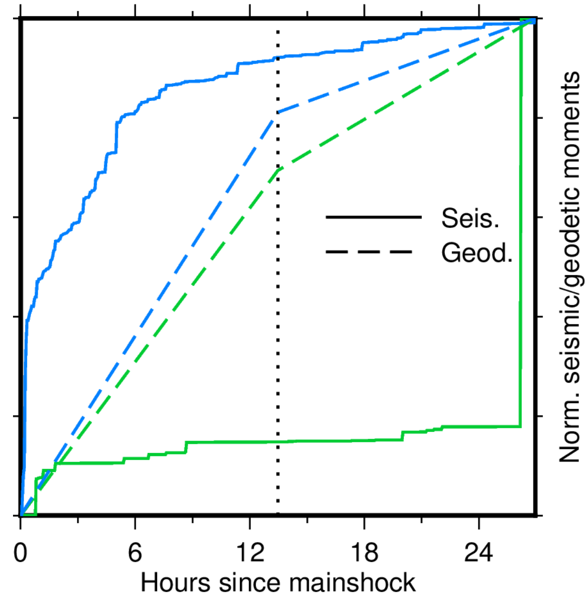

Figure S18. Same as Figure S2d but with the magnitude of the "M 6.1" event, described as M 5.6 in McBrearty et al. (2019) is not fixed to M_w 6.1 when calculating the seismic moment (See Main text)

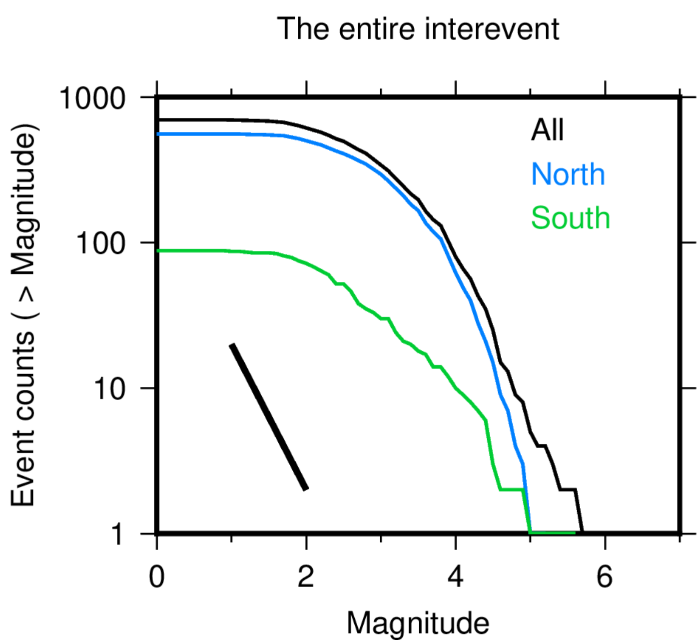

Figure S19. Gutenberg–Richter magnitude-count distribution curves during the interevent stage (Figure 2 and Section 2.3; McBrearty et al., 2019). Black lines indicate a slope of curves when the b-value of Gutenberg-Richter law is 1.0.

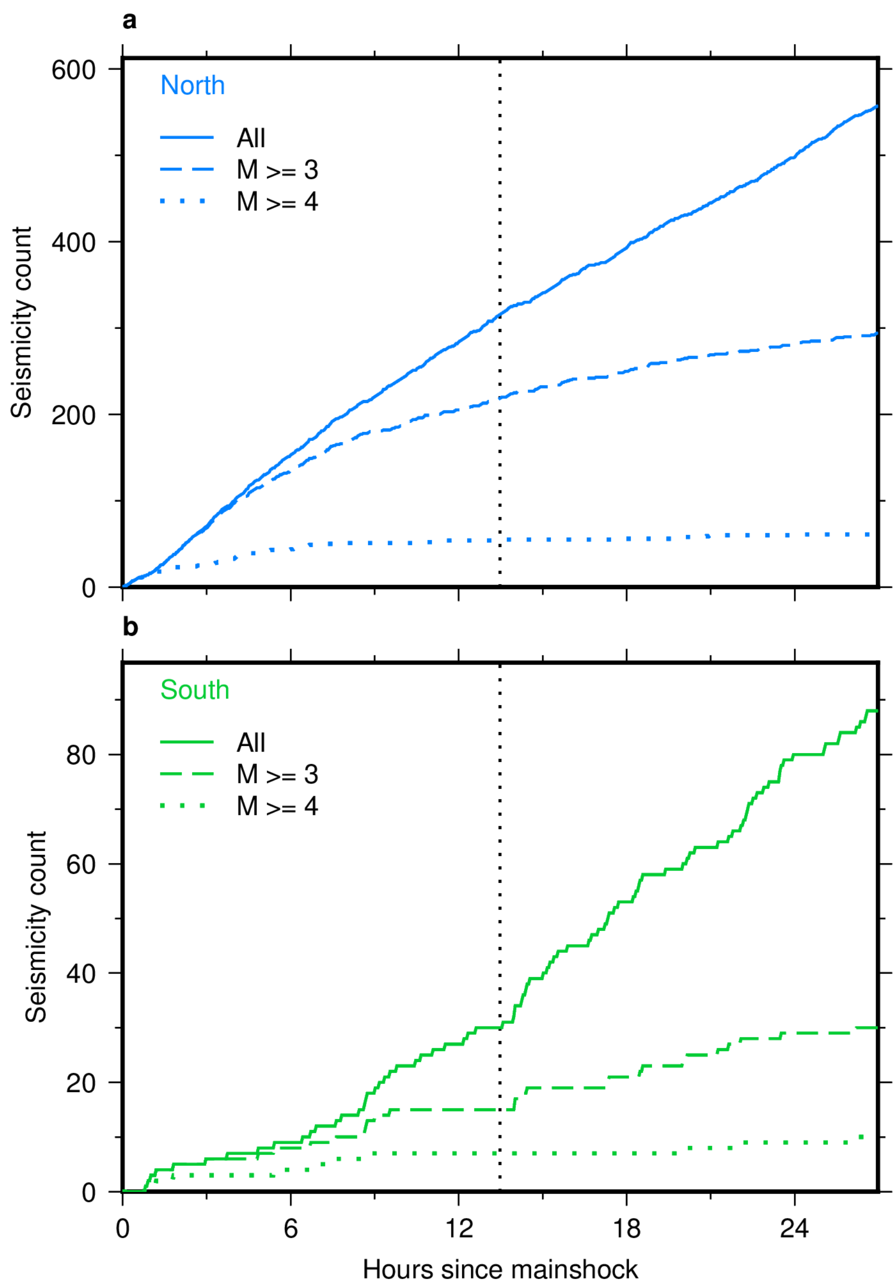

Figure S20. Interevent seismicity counts with all events (solid curves; same as Figure 2c) and those above magnitude 3 (broken curves) or 4 (dotted curves) in the North (a) and South (b) subregions.

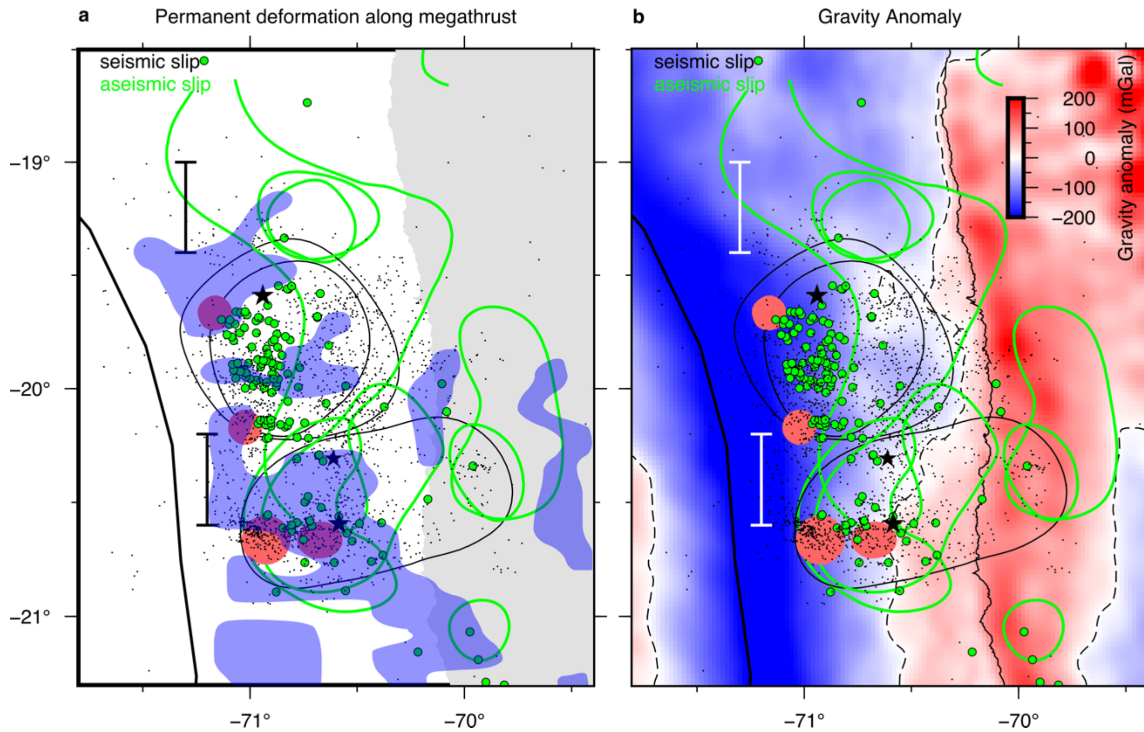

Figure S21. (a) Slip events at different stages with outlines of areas possibly hosting multiple faults subparallel to the megathrust (Cubas et al., 2022) (blue shapes). For clarity, seismic and aseismic slip events at different stages (Figure 4a) are drawn with black and green contours, respectively. Black dots are seismicity during the interevent and the post-largest-aftershock stages (McBrearty et al., 2019). (b) Same as (a) but with gravity anomaly (Sandwell et al., 2014) (background color) with zero value outlined with broken contours. Refer to Figure 1a for other elements.

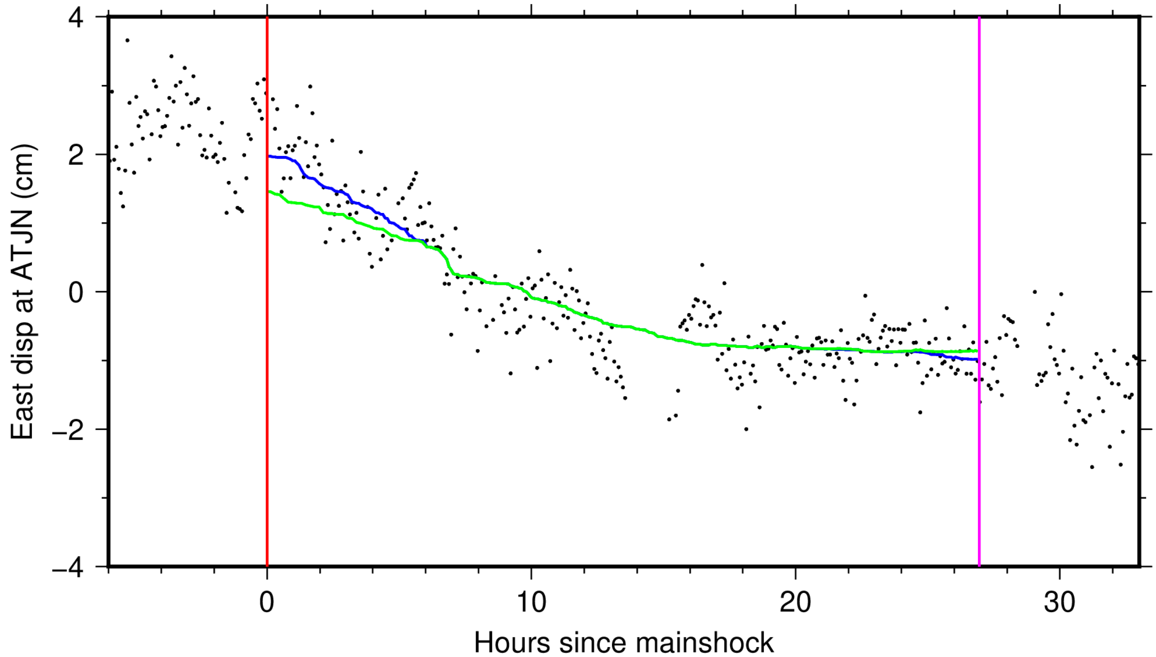

Figure S22. Comparison of moving median calculation with (blue) and without (green) data outside the interevent stage bounded by the mainshock (timing in red) and the largest aftershock (in magenta). The two coseismic steps (Figures S15a-b) are removed from the cleaned coordinates before calculating the moving median (black dots).

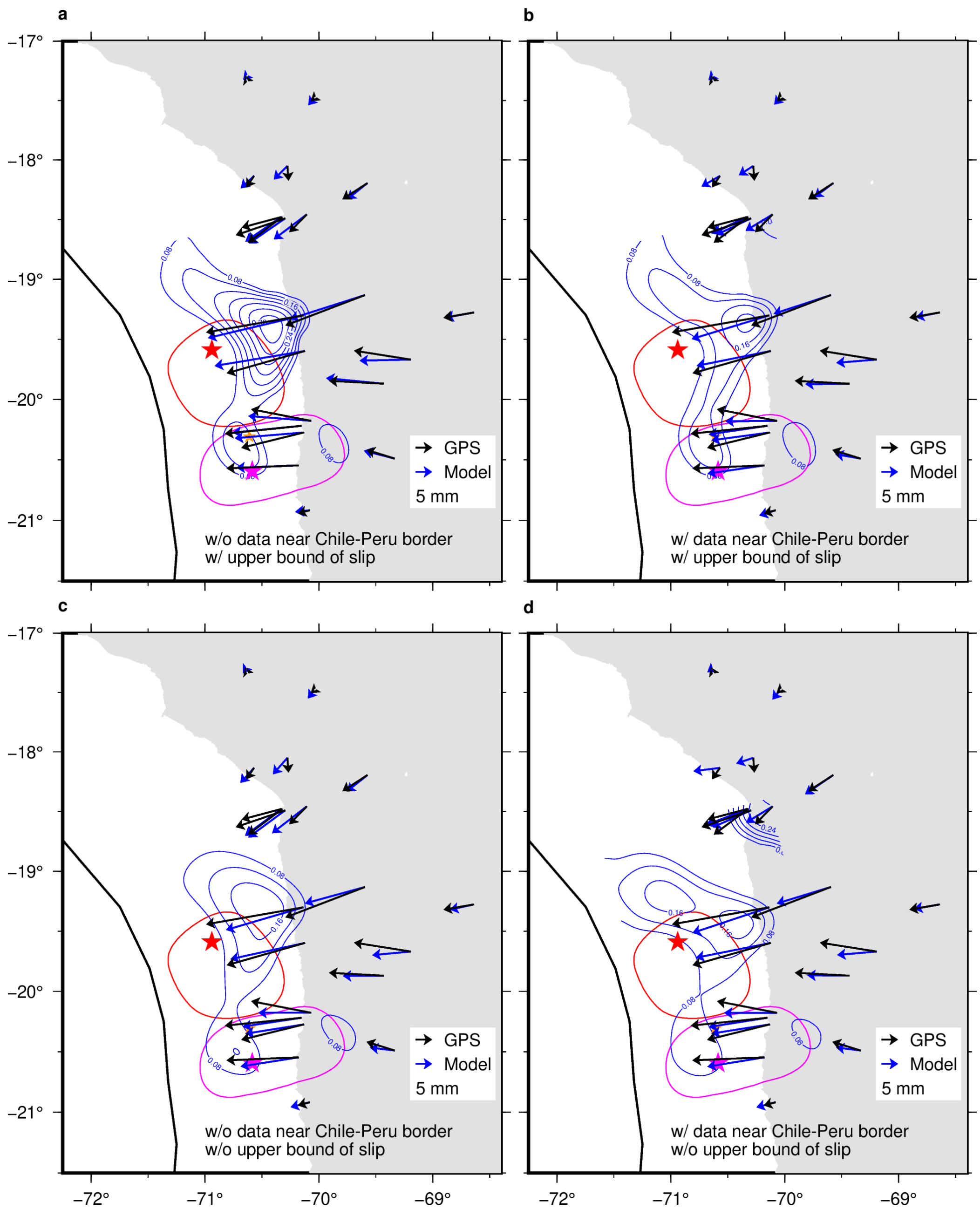

Figure S23. Slip inversions of the interevent cumulative displacement dataset derived from the moving median analysis (dataset (ii); See Text S4) with different settings. (a-b) The upper bound of slip amplitude (Figure 3a) is imposed and the data north of 19°S is included (a) or excluded (b). (c-d) The upper bound of slip amplitude is not imposed and the data north of 19°S is included (c) or excluded (d). See Figure 2e for other elements. Figure S23a is the same as Figure S17a.

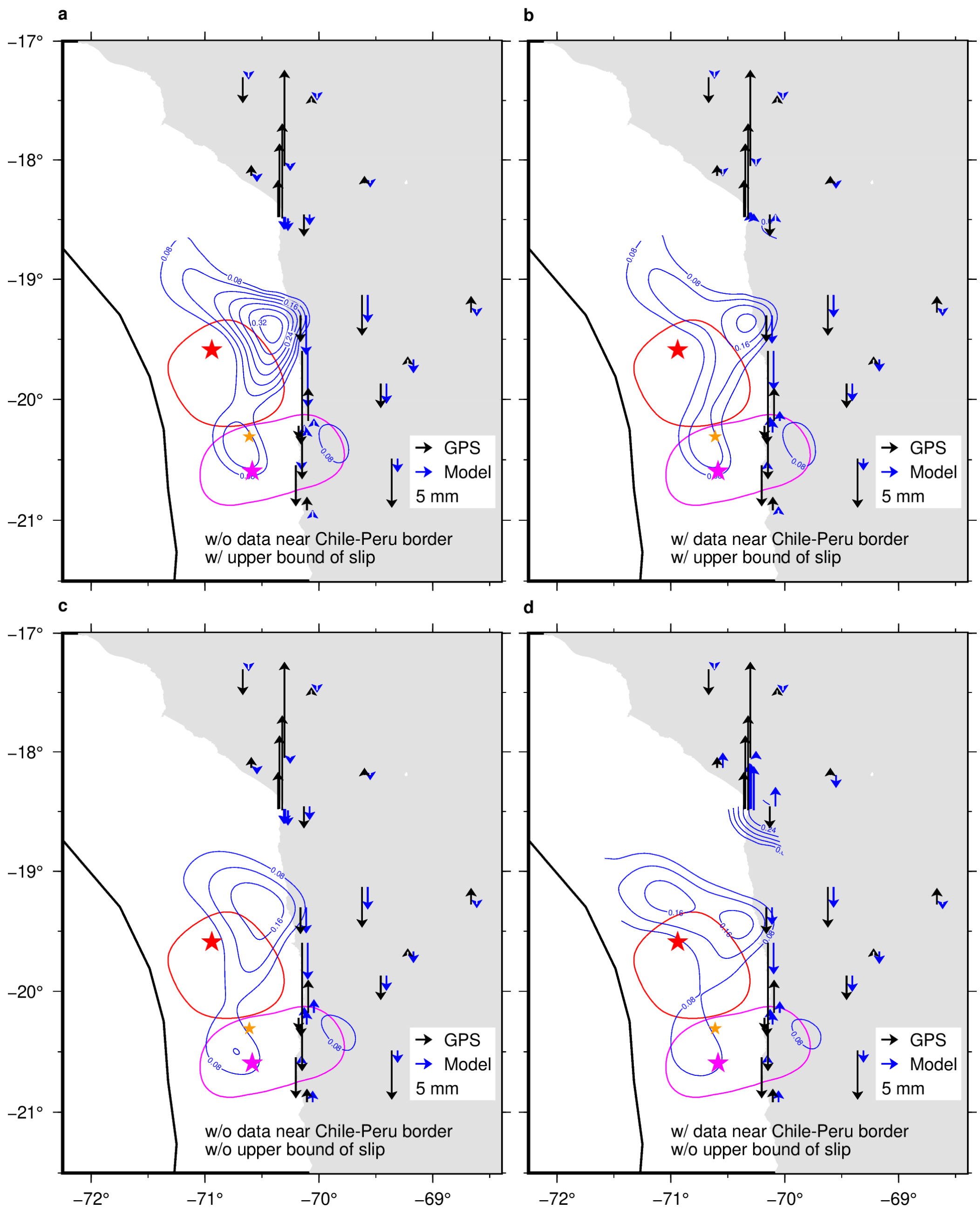

Figure S24. Same as Figure S23 but with the vertical data fit. Figure S24a is exactly same as Figure S17b.